# Target Design and Optimizations for Spent Fuel Transmutation

by

Grigor Tukharyan

B.S. Engineering Sciences, American University of Armenia, 2022

Submitted to the Department of Nuclear Science and Engineering
in partial fulfillment of the requirements for the degree of

MASTER OF SCIENCE IN NUCLEAR SCIENCE AND ENGINEERING

at the

MASSACHUSETTS INSTITUTE OF TECHNOLOGY

September 2024



| | |
|---|---|
| Authored by: | Grigor Tukharyan<br>Department of Nuclear Science and Engineering<br>August 18, 2024 |
| Certified by: | Areg Danagoulian<br>Associate Professor of Nuclear Science and Engineering, Thesis Supervisor |
| Certified by: | Benoit Forget<br>KEPCO Professor of Nuclear Science and Engineering<br>Department Head, Thesis Supervisor |
| Accepted by: | Ju Li<br>Professor of Nuclear Science and Engineering<br>Graduate Officer, Department of Nuclear Science and Engineering |

# Target Design and Optimizations for Spent Fuel Transmutation

by

Grigor Tukharyan

Submitted to the Department of Nuclear Science and Engineering
on August 18, 2024 in partial fulfillment of the requirements for the degree of

MASTER OF SCIENCE IN NUCLEAR SCIENCE AND ENGINEERING

## ABSTRACT

There are six long-lived fission products (LLFPs) identified in nuclear spent fuel, which account for at least 99% of the long-term radiotoxicity once actinide recycling is completed. This thesis examines the feasibility of using proton beams to transmute LLFPs into shorter-lived or stable isotopes. While long-term storage for high-level waste would still be necessary, transmuting the LLFPs can reduce the volume of waste material that needs to be stored.

The objectives of this research are to explore the design of a proton transmutation facility, as well as to determine the optimal LLFP target-blanket material configuration for maximizing the transmutation efficiency. This thesis analyzes the use of intermediate energy beams of 18-70 MeV from commercial cyclotrons for transmutation. This thesis also analyzes the use of 1000 MeV proton beams to generate a substantial number of secondary neutrons through spallation interactions with target materials. The secondary neutrons produced from the spallation process are utilized by the LLFP materials, while surrounding blanket materials are selected to enhance the transmutation efficiency.

PHITS, a Monte Carlo transport code, is employed to computationally model the interactions between LLFP materials and the proton beam. In this thesis, PHITS is used to estimate the flux-energy spectrum and the number of atoms irradiated in the LLFP target during beam interaction. This data is then post-processed using a 0-dimensional analysis in FISPACT to estimate the transmutation rate for each LLFP. PHITS is also used to find the depletion rate of the LLFPs for the 18-70 MeV beam case and for spallation-induced transmutations in the 1000 MeV case. Geant4, a Monte Carlo transport toolkit, is used to calculate the production rate of particles attributed to the spallation process.

Analysis of the performance of commercial cyclotrons with energies of 18-70 MeV indicates that transmutation rates increase with higher proton beam energy. A cyclotron with a beam current of 10 mA and beam energy of 70 MeV running continuously can transmute $15.401 \pm 0.069$ g/year of Tc-99. However, Tc-99 is produced at a rate of approximately 8.54 kg/year in a 1 GW reactor, suggesting that a single commercial cyclotron beam is currently not viable for transmutation purposes.

A proposed tank design with a lead/Tc-99 target that is surrounded by LLFP pins and heavy water is considered for the spallation study. Although using Tc-99 as a target directly transmutes $0.893 \pm 0.002$ kg/year from transmutation attributed to spallation, using lead as a target instead approximately doubles the transmutation rates in the LLFP regions for almost all of the LLFP isotopes. In both cases, the depletion rate of the LLFPs is greatly increased compared to using a commercial cyclotron of 70 MeV. A proton spallation source

with a beam current of 10 mA and beam energy of 1000 MeV, using a Tc-99 target, achieves a transmutation rate of approximately 10.9 kg/year of Tc-99 in the LLFP pins through secondary neutrons produced by the spallation process. In contrast, using a lead target achieves a higher transmutation rate of around 20.0 kg/year of Tc-99 in the LLFP pins.

This work was supported by the DOE ARPA-E Project under the award number DE-AR0001578.

Thesis supervisor: Areg Danagoulian
Title: Associate Professor of Nuclear Science and Engineering

Thesis supervisor: Benoit Forget
Title: KEPCO Professor of Nuclear Science and Engineering
Department Head

# Acknowledgments

I would like to thank my supervisors; Professor Areg Danagoulian and Professor Benoit Forget for their help and support while I have been working on this thesis. Through them, I have gained a lot of experience and been provided with a lot guidance through the past two years which has helped shape this thesis. Thanks to my supervisors, I have been motivated and inspired to continue into the path of research and academia.

I would also like to thank the amazing NSE department at MIT for being continuously supportive and always answering my questions whenever it was needed. Without this support, this thesis may not have been possible to complete.

Finally, this journey would not have been complete without the support of my family and with the friends that I have made on the way. Although my time at MIT was relatively short compared to others, I have felt welcomed and a part of this great community.

# Contents

# List of Figures

# List of Tables

# Chapter 1

# Introduction

## 1.1 Motivation

Long-term nuclear waste storage and disposal remain significant challenges in the United States. Currently, nuclear waste is stored mostly in dry casks at nuclear power plants without a long-term storage strategy, which worsens public opinion on nuclear fission. There are six long-lived fission products (LLFPs) identified in nuclear waste, which may be responsible for at least 99% of the long-term radio-toxicity once actinide recycling has been completed [1]. This work will investigate the technical and economic feasibility of transmuting the LLFPs using proton accelerators.

The target materials in focus are the LLFPs identified by the Department of Energy (DOE): Tc-99, Cs-135, Zr-93, Sn-126, I-129, and Se-79 [1]. All of these isotopes possess half-lives on the order of 100,000 to 10,000,000 years. Proton transmutation could address the problem of long-lasting nuclear waste. Subjecting the isotopes to proton bombardment allows the generation of isotopes with shorter half-lives or stable isotopes. This process may significantly reduce or even eliminate the necessity for long-term storage of nuclear waste.

## 1.2 Previous Work

The previously mentioned LLFP isotopes will produce shorter lived or stable isotopes when they capture protons and go through (p,xn) reactions [2]. Making use of protons (and by-products) is preferable to neutrons produced from reactors which can offer high flux but will produce more fission products while the reactor operates. This thesis analyzes different types of accelerators used worldwide to design a potential transmutation facility. Proton cyclotrons are considered as best candidate for an accelerator to be used in this facility. Most of the cyclotrons sustain beam energies of 9-70 MeV [3], making them good prospects for transmutation purposes, as proton capture cross-sections for (p,n) and (p,2n) reactions are highest in the 9-30 MeV range. Spallation reactions will also be present within the 9-70 MeV range, but not as prevalent as with a 1000 MeV accelerator beam.

The elements in the spent fuel have various mass fractions. This thesis accounts for the fact that stable and unstable isotopes exist in the spent fuel [1]. The target materials utilized in this thesis, if not mentioned as a pure isotope, correspond to the isotopic composition

obtained from evaluation group 23, as outlined in the "Nuclear Fuel Cycle Evaluation and Screening" study [1]. For example, Table 1.1 below contains the initial isotopic compositions for elemental selenium in pressurized water reactor (PWR) spent fuel at a given burn-up.

Table 1.1: Initial isotopic composition for elemental selenium [1].

| Isotope | Half-Life (days) | Mass Fraction |
|---|---|---|
| Se77 | stable | 3.44% |
| Se78 | stable | 6.53% |
| Se79 | 1.08E+08 | 13.88% |
| Se80 | stable | 21.32% |
| Se82 | stable | 54.79% |

## 1.3 Objectives

The goals of this thesis are to investigate the design and the potential of a cyclotron transmutation facility and the optimal LLFP target-blanket material configuration for higher efficiency of transmutation. This thesis also analyzes the use of 1000 MeV proton beams for spallation to produce high quantities of neutrons that are created by the protons interacting with the target materials. The LLFP materials utilize secondary neutrons from the spallation process and surrounding blanket materials are selected to optimize transmutation. All of the research in this thesis will be computational, due to the nature of the topic and the difficulty to currently recreate the results experimentally.

As all of the work is computational, several Monte Carlo codes will be used in this thesis. PHITS (Particle and Heavy Ion Transport System) is a particle transport code that models the transport of particles over a wide range of energies [4]. Geant4 is object-oriented Monte Carlo transport code that can track particles and model the interactions they have through their environment [5]. Both of these tools will be used to achieve the goals for this thesis. The cross-section data utilized for the six identified isotopes will be acquired from the physics lists and models that are contained within Geant4 and PHITS.

## 1.4 Structure

The first section of this thesis concentrates on the use of intermediate energy protons to transmute the LLFPs. The energy spectra of the proton and neutron fluxes inside each material is collected as the proton beam passes through the target. The second section considers alternative methods for transmutation, including the use of high-energy beams for spallation and the use of blanket layers. Blanket layer materials are chosen based on their abilities to produce additional particles that can enhance transmutation or their ability to moderate neutrons. Each simulation takes into account contemporary accelerator technologies for beam size and energy; however, the use of future technologies to achieve higher

transmutation rates will also be taken into account. A companion thesis will use the flux data generated from the simulations for depletion analysis in FISPACT [6].

# Chapter 2

# Background

## 2.1 Long Lived Fission Products (LLFPs)

LLFPs are radioactive materials with long half-lives that exceed 100,000 years. These materials are produced in nuclear reactors as a product of nuclear fission of uranium or plutonium. Most of the LLFPs are beta-emitters, which complicates detection in the case of a leak or disaster [7]. The long-term radio-toxicity of the LLFPs require the isolation of these materials in waste storage for long periods of time. Out of all LLFP isotopes, Tc-99, I-129, Zr-93, Sn-126, Cs-135, and Se-79 contribute to more than 99% of the long-term radio-toxicity for any fuel cycle [1]. Table 2.1 below showcases the average radio-toxicity contribution for each isotope after 1000 years in different fuel cycle categories.

Table 2.1: Average isotopic contributions to radiotoxicity after 1000 years in each evaluation group category [1].

| Group | Tc-99 | I-129 | Sn-126 | Zr-93 | Cs-135 | Se-79 | Sum |
|---|---|---|---|---|---|---|---|
| Once-Through | $42.6 \pm 15.0\%$ | $22.1 \pm 4.4\%$ | $14.1 \pm 9.4\%$ | $11.3 \pm 2.7\%$ | $7.9 \pm 4.9\%$ | $1.8 \pm 0.8\%$ | $99.7 \pm 0.3\%$ |
| Limited-Recycle | $46.3 \pm 4.7\%$ | $21.1 \pm 4.8\%$ | $11.9 \pm 4.7\%$ | $11.2 \pm 1.6\%$ | $7.3 \pm 3.5\%$ | $1.8 \pm 0.7\%$ | $99.6 \pm 0.2\%$ |
| Continuous-Recycle | $44.1 \pm 6.3\%$ | $22.8 \pm 2.1\%$ | $12.4 \pm 5.2\%$ | $9.2 \pm 2.1\%$ | $9.4 \pm 4.2\%$ | $1.6 \pm 0.7\%$ | $99.6 \pm 0.2\%$ |

Once-through recycling refers to a nuclear fuel cycle in which spent fuel is not reprocessed. In contrast, limited-recycle fuel cycles involve reprocessing spent fuel once or a few times, while continuous-recycle fuel cycles repeatedly reprocess the fuel to recover as much fissile material as possible [1]. If the six listed LLFPs were to be removed from the waste stream, the long-term radio-toxicity attributed to LLFPs can be reduced by more than 99%. To achieve this, the LLFPs can be transmuted into stable or shorter-lived isotopes with the use of proton irradiation.

As seen above, Tc-99 contributes the most to radio-toxicity out of the six LLFPs. Tc-99 (11.5 g/cm$^3$) is the only isotope of technetium that is remains in nuclear reactor spent fuel. Around 60-80% of the Tc-99 material is found in a soluble form as $TcO_4$, which is relatively mobile in groundwater. Tc-99 is a beta-emitter with a half-life of 213,000 years and is a health risk if ingested. The soluble fraction of technetium can be transformed into metallic technetium and added to the insoluble fraction through reprocessing [8].

Similarly to Tc-99, Sn-126 occurs in both soluble and insoluble forms and emits energetic gamma radiation, but is produced in far less quantities than technetium in thermal reactors. Fast reactors may produce more Sn-126 from fast fission [8]. This thesis assumes that the LLFPs are separated from the rest of the nuclear spent fuel and correspond to an isotopic composition. Unlike Tc-99, many isotopes of tin are created within spent nuclear fuel. The half-life of each tin isotope as well as their mass fractions are listed in Table 2.2 below.

Table 2.2: Initial isotopic composition of tin (6.9 g/cm$^3$) [1].

| Isotope | Half-Life (days) | Mass Fraction |
|---|---|---|
| Sn-115 | stable | 0.4% |
| Sn-116 | stable | 5.57% |
| Sn-117 | stable | 9.55% |
| Sn-118 | stable | 9.76% |
| Sn-119 | stable | 9.81% |
| Sn-120 | stable | 9.78% |
| Sn-122 | stable | 10.69% |
| Sn-124 | stable | 14.82% |
| Sn-126 | 8.4E+07 | 29.57% |

Like tin, zirconium is also found in several isotopic forms (Zr-90, Zr-91, Zr-92, Zr-93, Zr-94, Zr-96). Zr-93 decays into an excited state of Nb-93 by emission of a beta particle, which will then decay a low-energy gamma ray to reach ground state. Research into separation techniques for zirconium are currently ongoing [8]. The initial isotopic composition of zirconium can be found below in Table 2.3.

Table 2.3: Initial isotopic composition of zirconium (6.5 g/cm$^3$) [1].

| Isotope | Half-Life (days) | Mass Fraction |
|---|---|---|
| Zr-90 | stable | 1.73% |
| Zr-91 | stable | 13.34% |
| Zr-92 | stable | 16.22% |
| Zr-93 | 5.59E+08 | 20.26% |
| Zr-94 | stable | 21.97% |
| Zr-96 | 7.31E+21 | 26.48% |

Se-79 is produced in the lowest quantity and contributes the least to radio-toxicity out of all the LLFPs. It can be found in vitrified waste and chemically behaves similarly to a sulphate [8]. Se-82 and Se-80 are stable isotopes of selenium that are produced in greater amount than Se-79 due to their higher fission product yields. The isotopes of selenium and their mass fractions are listed in Table 2.4 below.

Cs-135 has a long half-life of 2 million years but has the second lowest contribution to radio-toxicity out of the LLFPs. Cesium is very mobile and requires storage in a suitable material such as glass to prevent damage to the biosphere. Cesium is produced as 4 separate

Table 2.4: Initial isotopic composition of selenium (4.3 g/cm$^3$) [1].

| Isotope | Half-Life (days) | Mass Fraction |
|---|---|---|
| Se-77 | stable | 3.44% |
| Se-78 | stable | 6.53% |
| Se-79 | 1.08E+08 | 13.88% |
| Se-80 | stable | 21.31% |
| Se-82 | stable | 54.79% |

isotopes (Cs-133, Cs-134, Cs-135, Cs-137) in waste. This complicates neutron transmutation of Cs-135 as isotopes Cs-133 and Cs-134 can generate Cs-135 during irradiation [8]. The initial isotopic composition of cesium is listed in Table 2.5 below.

Table 2.5: Initial isotopic composition of cesium (4.5 g/cm$^3$) [1].

| Isotope | Half-Life (days) | Mass Fraction |
|---|---|---|
| Cs-133 | stable | 32.87% |
| Cs-134 | 754.32 | 0.33% |
| Cs-135 | 8.4E+08 | 38.06% |
| Cs-137 | 1.10E+04 | 28.74% |

Iodine is produced as two isotopes, I-127 which is stable and I-129 which is the LLFP. Around 95-98% of Iodine is stored as a gaseous effluent, but once dissolved is very mobile in groundwater. Due to its high mobility and the fact that the thyroid gland concentrates iodine, I-129 presents itself as a great bio-hazard. Iodine is likely to contribute the longest to radio-toxicity out of the LLFPs in storage due to its long half-life of 15.7 million years [8]. In this thesis, iodine will be modeled as a part of a CsI compound, as shown in Table 2.7. The mass fractions of both iodine isotopes can be found in Table 2.6 below.

Table 2.6: Initial isotopic composition of iodine (4.5 g/cm$^3$) [1].

| Isotope | Half-Life (days) | Mass Fraction |
|---|---|---|
| I-127 | stable | 27.85% |
| I-129 | 5.73E+09 | 72.15% |

In this thesis, the LLFP targets are made with the isotopic compositions listed above, with the exception of Tc-99. The inclusion of these isotopes in the target material complicate and reduce the transmutation rate of the LLFP isotopes. Tc-99 targets are assumed to be metallic where the soluble fraction is transformed into metallic technetium.

A CsI salt compound material is used as a target because it protects against iodine dispersing due to high mobility and the cesium being liquid at room temperature.

The CsI compound material utilizes the isotopic compositions of cesium and iodine as listed in Tables 2.5 and 2.6 above. Table 2.7 shows the chemical form each LLFP (except for technetium) is found in after separation from the spent nuclear fuel.

Table 2.7: LLFP target form and density [1].

| LLFP | Chemical Form | Target Density ($g/cm^3$) |
|---|---|---|
| Cs-135 | CsI Compound | 4.5 |
| I-129 | CsI Compound | 4.5 |
| Zr-93 | Zirconium Metal | 6.5 |
| Sn-126 | Tin Metal | 6.9 |
| Se-79 | Elemental Selenium | 4.3 |

## 2.2 Waste Transmutation Options

The transmutation of LLFPs using neutron irradiation require high fluxes, which has necessitated the use of nuclear reactors. Several studies have looked at the potential of the using different kinds of nuclear reactors for the use of transmutation.

### 2.2.1 Reactor Options

Light Water Reactors (LWRs) are abundant in the US and Europe, which makes them a sought out candidate for the use of neutron transmutation. Despite their abundance and with promisingly high neutron flux production, LWRs are incapable of transmuting Tc-99 faster than they produce it. LWRs require large inventories of LLFP material for high transmutation rates which cannot be achieved in practice [9]. Heavy Water Reactors (HWRs) were also analyzed for the use of transmutation. The most efficient Tc-99 transmutation rates were found when Tc-99 was diluted in the moderator between fuel bundles. Despite achieving a transmutation rate equal to the Tc-99 production rate of four LWRs with the same power, the technology to achieve this is difficult and also increases the fuel enrichment requirement for the HWR [9].

Advanced nuclear reactors such as fast reactors have also been considered for transmutation. Lead-cooled fast reactors can be configured to have LLFP assembly rods around the reactor's main fuel rods. The LLFPs can be transmuted efficiently in this assembly, with Tc-99, Se-79, and I-129 achieving self-sustained transmutation. The safety effects of adding the LLFP assemblies to the core are not well known however, and further research is required [10]. Fast reactors with both moderated and non-moderated sub-assemblies have been found to effectively transmute certain LLFPs. One study finds that a moderated sub-assembly fast reactor has the potential to transmute I-129 at a rate equal to the production rate of three 1000 MWe LWRs [11]. Another study suggests that a 1200 MWe moderated sub-assembly reactor can transmute the Tc-99 production from five 1000 MWe LWRs [9]. Without moderation, a fast reactor is capable of transmuting the Tc-99 production rate from four 1000 MWe LWRs. However, large inventories of LLFP material are required for efficient transmutation of LLFPs with fast reactors. Non-moderated and moderated assembly fast reactors would require 2.7 and 3.4 tonnes of Tc-99 respectively to achieve the aforementioned transmutation rates [9].

### 2.2.2 ADS Options

Accelerator-driven system (ADS) subcritical reactors work by coupling a spallation source with a subcritical reactor core. In ADS, high-flux neutrons are produced by spallation reactions on a lead target inside the core. These neutrons drive the fission chain reactions inside the nuclear fuel which are otherwise not sustainable without the input from the spallation source [12]. Due to the production of high-flux neutrons, ADS has been considered for transmutation purposes as well. The Advanced Nuclear Energy System (ANES) is a proposed concept for an ADS that uses a gamma ray beam to bombard a cesium and iodine target to produce intense photoneutrons. Assuming that ANES operates for 20 years at 500MWt, the photoneutrons are able to transmute 30% of several LLFPs (Tc-99, I-129, and Se-79) . However, the proposed gamma ray beam intensity is not yet achieved, being a few orders of magnitude higher than what is currently technologically supported [13]. A different study on I-129 transmutation using an ADS system finds that an ADS system could transmute I-129 at the same rate as the production rate of ten LWRs. This proposed ADS system requires the use of a 1.5 GeV proton spallation source with a beam current around 16-18 mA, which is not achievable with current technology [14].

## 2.3 Review of Accelerators

Although previous attempts of LLFP transmutation have involved the use of neutron irradiation, advances in accelerator technologies now provide new approaches to transmutation with the use of high-energy non-neutron particles.

### 2.3.1 Photon Transmutation

Previously, non-neutron transmutation research has been limited due to the lack of higher energy non-neutron sources. However, there have been many advancements in accelerator technology, allowing the use of higher energy photons and protons for transmutation purposes. High energy photons can be created with the use of electrons and lasers. By introducing an intense laser to the electron beam, energetic gamma-rays are created by the process of Compton scattering. The energy of the gamma-ray can be configured by changing the wavelength of the laser and the energy of the electron beam. These gamma-rays will then induce a resonance of the target which will emit a photoneutron [15]. Bremsstrahlung photons from a laser can also be used for transmutation. However, a previous study found that the transmutation rates with the use of Bremsstrahlung photons is four orders of magnitude lower than with the use of Compton back scattering photons, which is increased to five orders of magnitude when using the ENDF/B-VII library [16]. Transmutation of Tc-99 is complicated when using photon irradiation however, due to the nature of the photonuclear reactions. The Tc-99 ($\gamma$,n) and the Tc-99 ($\gamma$, 2n) reactions will produce Tc-98 and Tc-97 respectively, which have longer half-lives than Tc-99 [16]. Conversely, Proton irradiation of Tc-99 does not have the same problem. The Tc-99 (p,n) and the Tc-99 (p,2n) reactions will produce Ru-99 and Ru-98 respectively, which are both stable isotopes. As seen in Table 2.1, the isotopic radiotoxicity contribution after 1000 years is the highest for Tc-99. This suggests

that protons are preferable to photons for LLFP transmutation. This thesis is a part of a larger study where multiple options for LLFP transmutation are considered. However, this thesis will concentrate on the use of protons to either transmute the target directly, or to be used as a spallation source to generate high neutron flux.

### 2.3.2 Proton Transmutation

#### Cyclotron Review

There are several accelerator options for the purpose of proton transmutation which include linear accelerators, cyclotrons and synchrotrons. To find the best option for this thesis's purposes, the availability of the accelerator type is considered. As previously mentioned, the proton capture cross-sections for (p,n) and (p,2n) reactions are the highest in the 9-30 MeV range for the LLFPs. Many proton cyclotrons are available that can produce 9-70 MeV protons, and can utilize the high (p,xn) cross-sections [3]. There is a large commercial market for proton cyclotrons due to their use in particle therapy and radioisotope production [17]. This removes the requirement of creating a proton accelerator from scratch and the reduces fabrication and design costs of the transmutation facility.

Proton accelerators work by creating an electric field to achieve acceleration of the charged proton particles. Repetitive crossing of electric-field regions in gaps between electrodes accelerates particles that traverse through these gaps. The core concept behind the linear accelerator is a row of such electrodes. In order for the same gap to be traversed repeatedly, a homogeneous magnetic field is used to bend the particles a long a circular trajectory. This allows the reuse of the same acceleration gap and reduces the cost and dimensions required to achieve high beam energy. This configuration was called the "magnetic resonance accelerator" which is now known as the cyclotron [17]. A typical cyclotron has several important components required for functionality. The proton source is located in the center of the cyclotron which ionizes hydrogen gas to extract protons. An RF system accelerates the protons between the electrode plates (also known as "Dees") with a strong electric field, while a powerful magnet restricts their trajectories into a spiral-shaped orbit. This allows the RF voltage between the electrodes to repeatedly accelerate the proton particles. An extraction system directs the particles that have reached their maximum energy into a beam-transport system to exit the cyclotron [17]. Figure 2.1 below showcases the typical design of a cyclotron as seen from the center region.

In the pictured cyclotron, the ion source is made up of two cathodes at each end of a vertical hollow cylinder at ground potential, which are positioned above and below the cyclotron's median plane. The cathodes and their opposing grounded anodes get filled with hydrogen gas. Random electron emission from the cathodes in the strong electric field between the cathode and the ground generates free electrons. The electrons are driven toward the anodes in the electric field, ionizing the gas in the process. The cathodes are struck by the ionized gas atoms, which causes them to release even more electrons. The gas is further ionized by the electrons and ions, which are trapped in gyroscopic orbits along the vertical magnetic-field lines and jump up and down between the cathodes. The space between the cathodes in the chimney gets filled with plasma made up of the electrons and ions. The closest Dee edge's electric field will pull and accelerate protons that have

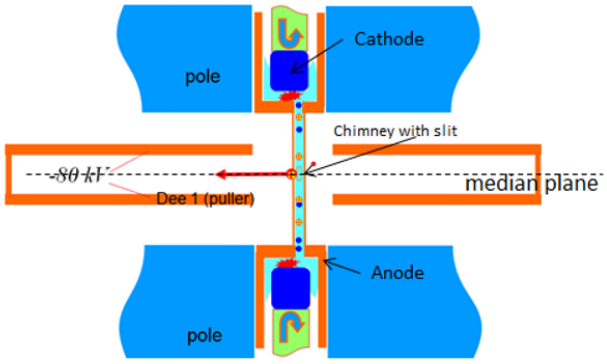


Figure 2.1: Typical cyclotron design adapted from ref [17].

escaped from the plasma. Only a small portion of the protons departing from the source are however accelerated, because of the small acceptance windows in both time and the further acceleration path [17]. Table 2.8 below shows commonly used commercial cyclotrons and their characteristics.

Table 2.8: Review of commonly used commercial cyclotrons [3].

| Company | Model | Beam Energy (MeV) | Beam Current (mA) |
|---|---|---|---|
| IBA | Cyclone Kiube | 18 | 0.10-0.30 |
| IBA | Cyclone 30 | 15-30 | 0.40-1.20 |
| IBA | Cyclone 70 | 30-70 | 0.75 |
| GE | PETtrace 800 | 16.5 | 0.06-0.16 |
| GE | PETtrace 800 | 16.5 | 0.06-0.16 |
| ACSI | TR-24 | 19-25 | 0.20-0.75 |
| ACSI | TR-30 | 15-33 | 0.75-1.60 |
| Sumitomo | MP-30 | 15-30 | >0.40 |

Transmutation is greatly dependent on the amount of proton flux generated by the cyclotron. This is dependent on the size and current of the outgoing proton beam. The desired beam energy of a cyclotron determines the maximum beam current that can be achieved with modern technology. In this thesis, a beam current of 10 mA is used for the Monte-Carlo computations based on the assumption that accelerator and RF technology will continuously develop over time. Facilities that can support a beam current of 10 mA and beam energies of 18-70 MeV do not exist currently in 2024.

### Cyclotron Cost Per Proton

When investigating the feasibility of creating a transmutation facility, it is important to ensure the chosen method is economically viable. The cost of operating a proton beam can be estimated by examining the power requirements of a cyclotron. If a facility were built with beam current of 10mA, it would produce $6.25 \times 10^{16}$ protons/second. The commercial electricity rate in Massachusetts in 2024 is 17.47 ¢/kWh. Table 2.9 demonstrates the estimated

annual electricity cost and cost per proton for cyclotrons.

Table 2.9: Estimated annual electricity cost & cost per proton for 1mA beam cyclotrons.

| Beam Power (MeV) | Power Consumption[18] | Annual Electricity Cost | Cost per Proton |
|---|---|---|---|
| 30 | 397 kW | \$ 600K/year | \$ $3.08 \times 10^{-19}$ |
| 45 | 561 kW | \$ 858K/year | \$ $4.36 \times 10^{-19}$ |
| 70 | 831 kW | \$ 1270K/year | \$ $6.45 \times 10^{-19}$ |

Note that power consumption is only considered for the cyclotron, and does not include power for other facility functionality. Increasing the beam power linearly increases the annual electricity cost for running the cyclotron. Power consumption is assumed from DOE estimates for 1mA beam cyclotrons, for 10mA these would be higher and the annual electricity cost would increase. The DOE estimates do not mention power to grid efficiency for the power consumption requirements [18]. Finding the cost of operating the beam line is useful for finding the cost of transmutation. This is discussed further in the Results and Discussion section of this thesis.

### Spallation Source Review

Spallation is a process in which highly energetic particles such as protons (above 100 MeV) interact with a nucleus and as a result emit nucleons. The emission of the nucleons from the atomic nucleus greatly reduces its atomic weight. As seen in figure 2.2 below, the incoming particle reacts with the nucleons inside the nucleus which create an intranuclear cascade of highly-energetic (more than 20 MeV) particles within the nucleus. During this process, some of the protons and neutrons escape the nucleus as secondary particles while others excite the nucleus by depositing their kinetic energy. The nucleus will reach ground state by emitting low energy particles that have less than 20 MeV energy in a process known as nuclear de-excitation. Most of these emitted particles are neutrons. The highly-energetic secondary particles that escape the nucleus can collide with other nuclei in the target as they travel in approximately the same direction as the spallation source. These particles will then cause secondary spallation reactions in the surrounding nuclei due to their high energy. This further generates more secondary particles and emit low energy neutrons in a process known as the hadronic cascade. Spallation differs from fission by the energy distribution of emitted particles and the number of neutrons released from reactions. Spallation neutrons are more energetic than fission neutrons, as the secondary neutrons released from the nuclei can nearly match the energy from the incoming spallation source. Fission reactions produce considerably less neutrons than spallation reactions. While the average number of neutrons released in a fission event is around 2.5, a single 800 MeV proton can release 13 neutrons from a tungsten target in a spallation reaction [19].

There are several facilities involving spallation sources around the world. The Spallation Neutron Source (SNS) is currently the world's most powerful accelerator pulse spallation source. At the front-end of the facility, an ion source produces negatively charged hydrogen ions which are then accelerated to an energy of 1 GeV by a linear particle accelerator. These ions are then stripped of their electrons to produce protons by passing through a foil. The

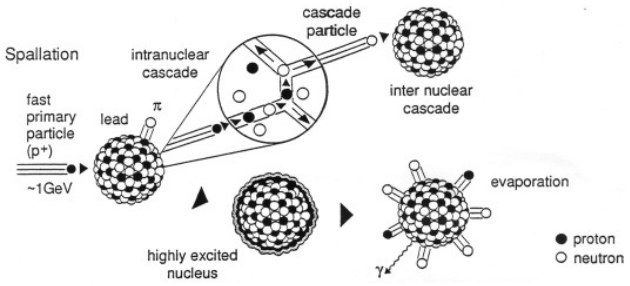


Figure 2.2: Schematic representation of the spallation process on a heavy nuclei adapted from ref [20].

protons then travel to an accumulator to amplify the current and release the protons through pulsed batches. To produce neutrons, the pulsed protons are released into a liquid mercury target where they undergo spallation. A moderator is used to slow down the neutrons generated from the spallation process and are guided into several beam lines [21].

Another facility that uses spallation is the PSI high intensity proton accelerator. This facility is composed of three accelerators in series, the Cockcroft-Walton pre-accelerator, the Injector II cyclotron, and the Ring cyclotron. The protons are initially created in the pre-accelerator and are sent to the Injector II cyclotron where they are accelerated to 72 MeV. When the protons leave the Injector II cyclotron and enter the Ring cyclotron they are further accelerated to 590 MeV with a beam energy of 2.4 mA. The beam is then directed to the Swiss Spallation Neutron Source facility where neutrons are created by the energetic proton beam interacting with a spallation target. The target itself is composed of a matrix of lead filled Zircaloy tubes. The neutrons created by the process are moderated by heavy water surrounding the target and are transferred to one of 13 instruments in the facility [22]. For this thesis, the spallation source will have a beam current of 10mA (to compare with the 18-70 MeV cases) and a beam energy of 1000 MeV, assuming that the technology to support such a beam will soon be realized.

### Spallation Source Cost Per Proton

For a 1000 MeV proton beam with a beam current of 10 mA, the beam power is projected to be around 1000 kW. However, the power grid to beam efficiency in such a system is around 13%, which increases the total power consumption of the system to 7700 kW [23]. Assuming that the commercial electricity rate is 17.47 ¢/kWh, the total annual electricity cost is $11,780k per year. Accounting for the beam energy of 10 mA, the cost of a single proton is $\$ 5.98 \times 10^{-18}$. The power grid to beam efficiency may be higher than 13% when the beam energy is 10 mA, potentially decreasing the costs of operation for the accelerator [23]. See the Results and Discussion section for further economic analysis.

# Chapter 3

# Methodology

## 3.1 Computational Methods

### 3.1.1 PHITS

PHITS (Particle and Heavy Ion Transport System), a Monte Carlo particle transport code designed to accurately simulate the transportation of radiation in different mediums is used extensively in this work [4]. PHITS is capable of modeling the intricate interactions between particles, heavy ions, and matter, encompassing nuclear reactions and electromagnetic processes. PHITS has a wide field of application fields which include spallation neutron sources, heavy ion therapy, space radiation, radiation shielding, and more. PHITS is distributed as a single package that contains its source, data-library, and executable files. As PHITS is a three-dimensional Monte Carlo transport code, it requires its user to set the geometry design inside the program. An estimate of the mean of a variable of interest can be deduced in PHITS with the use of tally estimator functions [24]. For this thesis, PHITS is used to calculate the penetration depth of proton beams in a target, analyze particle flux spectra, and to calculate the depletion rate of the LLFP materials.

#### Penetration Depth

The LLFP mass fractions are used to find the specific number density of each isotope within the isotopic composition. To determine the count of LLFP atoms irradiated by the proton beam, it is necessary to acquire the maximum penetration depth of the beam within the target. The maximum penetration depth is defined as the point where the flux of the incoming beam approaches zero for the 18-70 MeV runs. For the 1000 MeV case, the penetration depth is determined by the point where the beam flux diminishes by three orders of magnitude compared to the initial starting flux which can be seen in the Results and Discussions section. The identified targets undergo exposure to proton beams with energies of 18-70 MeV for the commercial cyclotron analysis and 1000 MeV for the spallation analysis. The penetration depth is recorded by analyzing the distances traveled by the protons within the targets. Protons with energies below 13 MeV are omitted from the 18-70 MeV simulation runs since they are essentially below the threshold of most reactions of interest. PHITS presents flux data in units of flux per source. To obtain results proportional to the beam

intensity, the data is multiplied by a normalization factor that corresponds to the selected beam current. The volume of the irradiated region of the target is calculated by $x\pi r^2$, where r represents the radius of the target and x represents the maximum penetration depth of the beam in the target. Subsequently, the volume of the irradiated region within the target and the number density (N) of the specific isotope in the target, are used to calculate the total number of atoms (n) of said isotope subjected to irradiation, as seen below.

$$n = Nx\pi r^2 \tag{3.1}$$

**Flux-Energy Spectrum**

As the proton beam traverses the target material, it undergoes attenuation. While the proton beam itself is mono-energetic, the flux experienced by the target material is not. It is crucial to consider the flux spectrum in order to analyze the characteristics of the flux, as the calculation of the transmutation rate relies on the energy-dependent cross section. PHITS can calculate the flux-energy spectrum inside of a target by using a tally function. Each simulation will contain a target of the same thickness as the full penetration depth of the proton beam during the atom count runs. The neutron and proton flux is collected throughout the geometrical mesh of the material for each target and energy configuration.

**Depletion Analysis**

When a proton beam interacts with a target, the subsequent reactions will deplete the LLFP isotopes within the target material. The T-Interact tally in PHITS allows the user to find the number of interactions within a specified volume in a simulation. This tally is used in this thesis to find the number of transmutations per unit volume inside the target volume when exposed to an incoming proton beam. The total LLFP mass transmuted in a year is found by knowing the current of the incoming beam and the average transmutations per volume. The results are used to compare with FISPACT's depletion analysis from the companion thesis, and can be found in the Results and Discussion section of this thesis.

### 3.1.2 Geant4

Geant4 is a Monte Carlo toolkit that simulates the passage of particles through materials like PHITS [5]. It's application fields include high energy accelerator physics, astrophysics, radiation protection. Geant4 offers the ability to individually track each particle within the simulation as well as the secondary particles that are created from reactions. Geant4 was developed out of the necessity of adding new physics models to a simulation system without adding the complexity that comes with procedure-based code. Geant4 instead uses object-oriented C++ code to limit dependencies and allows the user to create their own computational framework. The toolkit allows the user to create geometrical models and to simulate detectors by defining sensitive volumes [25]. Geant4 is used in this thesis to calculate particle production rates and to analyze individual particle tracks.

#### Particle Production

Geant4 is used to find the production rates of particles within a simulation. As Geant4 analyzes individual tracks, it allows the user to find the processes responsible for creating particles in each run. In this thesis, Geant4 is used to find the ratio of secondary neutrons created per incoming proton for the proton-induced spallation case. The processes that create the secondary neutrons (such as proton and neutron inelastic collisions) are also tracked to better understand the underlying dynamics of the system.

### 3.1.3 Other Computational Methods

#### FISPACT

FISPACT is a library database and inventory code that is designed to simulate depletion and transmutation processes resulting from nuclear reactions [6]. This code system is also able to model the time independent inventory of irradiated nuclides. FISPACT is comprised of three components, the main software for depletion and transmutation, nuclear data libraries, and validation/verification tests. The nuclear data libraries are ENDF6 formatted group cross-sections, with the option of user added libraries. The beam flux spectra, target nuclide count and composition, irradiation time, and particle type are used as inputs in PHITS and outputs activity, produced nuclide inventory, radiotoxicity, and more. FISPACT will be used in a companion thesis, where the flux-energy spectrum and number of irradiated atoms from the PHITS simulation results will be used as an input to calculate the LLFP transmutation rate. The results are compared with PHITS's depletion analysis in the Results and Discussion section.

## 3.2 Nuclear Data

Unfortunately there is a sparsity of experimental data for proton-induced cross-sections for all of the LLFP isotopes. The only exception is the (p,3n) cross-section for Tc-99, which has been verified experimentally in the 20-100 MeV range [26]. However, both PHITS and Geant4 contain physics models and evaluated data libraries which are mentioned below.

#### PHITS

The physics models in PHITS contain reaction cross-sections required for the LLFP isotopes. Figure 3.1 below showcases the recommended physics models for use in PHITS.

For neutrons above 10E-5 eV and under 20 MeV, the JENDL-4.0 data library is used with applications in fission and fussion systems. This library is used to simulate the low-energy neutron-induced reactions that occur within the simulations. The Liège Intranuclear Cascade model (INCL) is used for neutrons above 20 MeV and protons above 1 MeV. The INCL model is the main physics model used in this thesis, as it is currently one of the most accurate existing intra-nuclear models. It is able to accurately predict the emission of secondary particles and their energy distributions that result from spallation reactions.

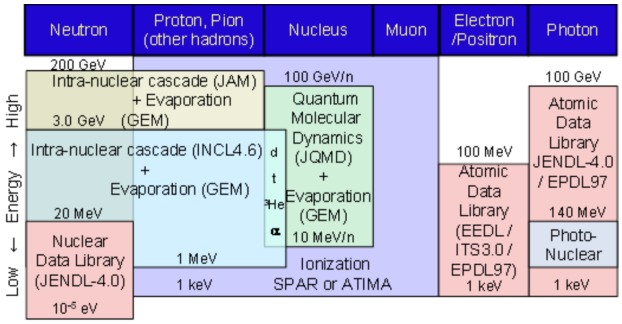


Figure 3.1: Physical models included in PHITS from ref [27].

GEM is used in tandem with INCL to simulate the evaporation and fissions that occur from hadron and nucleus-induced reactions [27].

### Geant4

Similarly to PHITS, Geant4 can be configured to use the INCL++ model (which is functionally the same as INCL4.6). Figure 3.2 below shows the map of INCL++-based models that are currently in use in Geant4 (for v10.1$\beta$).

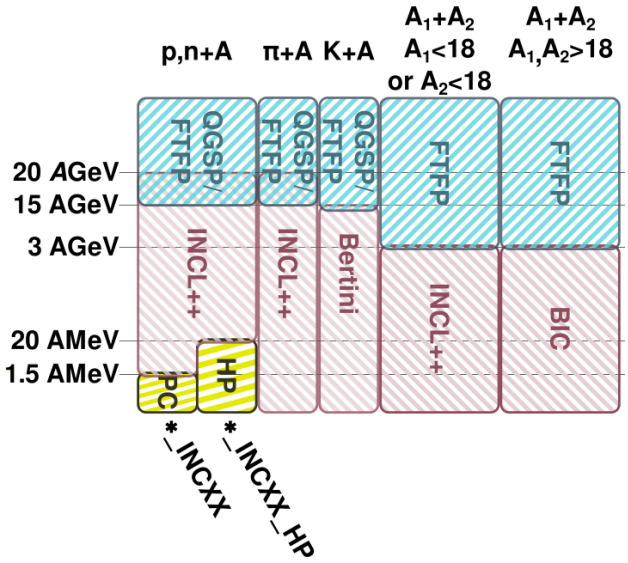


Figure 3.2: INCL++-based Geant4 physics lists from ref [28].

The INCL++ model is used to simulate nucleon and pion-induced reactions up to 15-20 GeV. For nucleon-induced reactions below 1-2 MeV the Precompound model is used instead. For simulating low energy neutron elastic and inelastic scattering, evaluated data libraries from the NeutronHP model are used [28].

## 3.3 Intermediate Energy

For the Intermediate Energy analysis, PHITS is used for all of the simulations. PHITS is utilized to simulate the interactions between a cyclotron proton beam and the aforementioned target materials. Each LLFP target will undergo exposure to proton beams with energies of 18, 23, 30, 50, and 70 MeV to find the penetration depth and number of irradiated atoms of said beams in the targets. As previously mentioned, the identified LLFP elements are found with a certain isotopic composition and these mass fractions are used to find the specific number density of each isotope (Table 1.1). Protons lose energy as a function of distance when interacting with a material. Thus, a study on the energy spectrum within the target helps characterize the proton flux characteristics. The flux spectrum of the neutrons within the target is also analyzed, as there is an abundant amount produced from (p,xn) reactions [2]. The data of the energy spectrum characteristics and the number of atoms irradiated are also used in the companion thesis for FISPACT, where a 0-dimensional analysis of each material will be used to perform transmutation calculations.

## 3.4 Spallation

An alternative method of transmutation is using the protons and neutrons produced by spallation. The first step in producing fast neutrons is the process of 1000 MeV proton beams interacting with neutron rich materials. These fast neutrons will then transmute LLFP targets around the neutron rich material. Geant4 is used initially for its ability to individually track all particles that exist in this simulation, and to quantify the number of neutrons and protons that are produced from the spallation process.

Work is done to find the best target and blanket material combination for the highest efficiency of transmutation. The target and blanket materials are made out of LLFP materials, but other materials are also considered for their neutron-rich qualities or moderating capabilities. To find the best target material, each candidate is analyzed separately in PHITS to find their proton and neutron flux spectra, as well as the number of irradiated atoms. Different beam and target radii are compared to find the optimum combination for transmutation. As mentioned previously, the data is used in FISPACT to find the transmutation rate for each material with their respective beam and target radii. Blanket layers made from LLFP materials utilize the neutron and proton flux exiting the target volume, yielding higher transmutation rates. Blanket materials with high (n,p) cross-sections such as beryllium are also studied to further increase the number of protons by utilizing the secondary neutrons from the target. The flux from the chosen target and blanket materials will also be geometrically examined using PHITS to understand where to place additional LLFP material around the target-blanket configuration. Moderator material in between layers may also be considered to slow down fast neutrons, to increase the likelihood of interactions between the neutrons and the LLFP materials.

# Chapter 4

# Results and Discussion

## 4.1 Intermediate Energy Analysis

### 4.1.1 Preliminary Analysis

PHITS has been utilized to irradiate a target and access the resulting proton and neutron fluxes. Preliminary results from a 30 MeV beam directed towards a target have demonstrated the ability to simulate neutron production. The target is a cylindrical elemental selenium target that is 1.0 cm long and has a radius of 0.1 cm, which is also the radius of the incoming proton beam. The proton and generated neutron fluxes are shown below in Figure 4.1 on the left and right respectively.

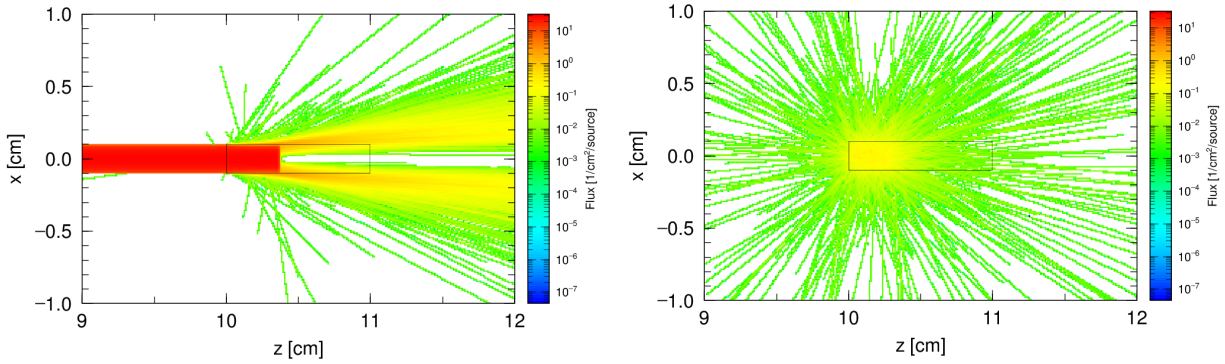


Figure 4.1: Two-dimensional analysis of flux per source for Protons (left) and Neutrons (right) on an elemental selenium target with a 30 MeV proton beam.

The flux is listed in units of $1/(\text{cm}^2/\text{source})$, where source refers to the normalization factor attributed to the 10 mA beam current. In this case, the normalization factor has not been applied to the results. As seen above, the incoming proton flux doesn't travel far into the target. Some of the proton flux is also scattered outside of the target at this point, meaning it is not being utilized to its full potential. Neutrons are created as a result of the proton irradiation, but the neutron flux is 3 to 4 orders of magnitude lower than the proton flux. Figure 4.2 below shows the flux per source in the z-direction of a 2 cm long cylindrical

elemental selenium target with a 70 MeV proton beam, where the target geometry starts at 10.0 cm on the z-axis.

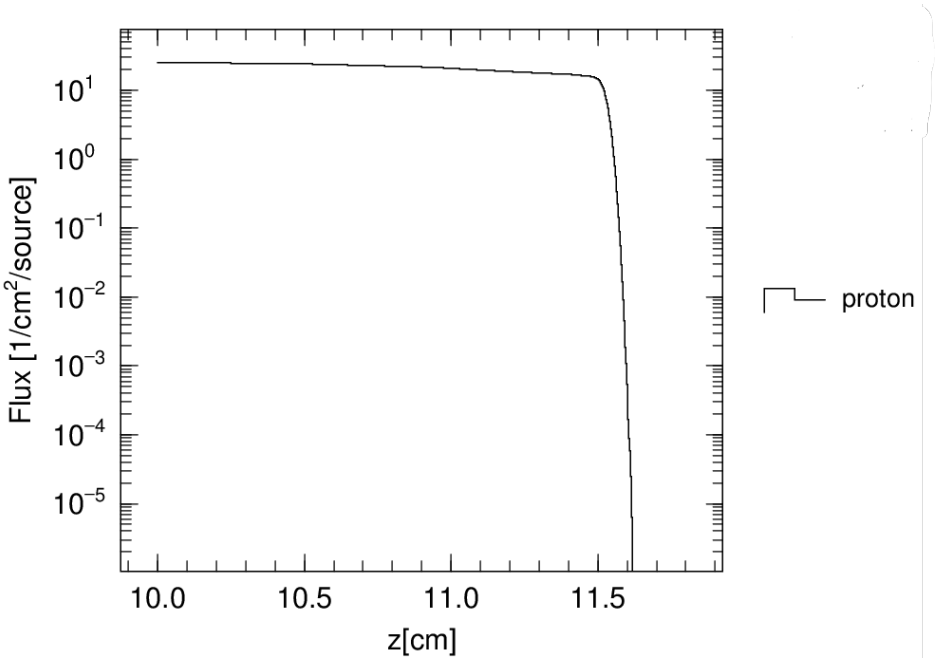


Figure 4.2: Flux per source penetration analysis inside an elemental selenium target with a 70 MeV proton beam, note that 10 cm on the z axis is where the target area begins.

Protons have a positive charge, which makes them interact strongly with the nuclei and the negatively charged electrons of the atoms in the target material. As a result, the proton flux drops sharply after travelling a certain distance inside the target. Most of the deposited energy is localized to where the proton beams initially interact with the target, and said protons have trouble penetrating the target. This suggests a few concerns, that very few atoms will see a sufficiently high flux inside a large target, and large amounts of heat will deposit on the target surface.

### 4.1.2 LLFP Penetration Depth

To calculate the transmutation rate of the target material in FISPACT, it is necessary to determine the number of atoms exposed to the proton flux. Finding the maximum penetration depth of a proton beam at a given energy in a LLFP material will also be helpful in creating a target design that fully utilizes the incoming proton beam. As mentioned previously, the maximum penetration depth is considered at the point where the proton flux abruptly drops inside a target geometry as seen above in Figure 4.2. Using PHITS, the beam and target radii are set as 0.1 cm, while the target length is long enough to fully capture the incoming proton beam. The distance from the start of the target volume and where the proton flux drops to zero is recorded and used to find the volume of irradiated region, which is used to find the number of irradiated atoms inside the target. Tables 4.1-4.6 below showcase the penetration depth of a proton beam at a given energy inside each of the elemental LLFP

targets. They also provide the total number of elemental atoms and the number of the LLFP isotope atoms that are irradiated by the proton beam. Table 4.6 does not provide the total number of irradiated elemental atoms as Tc-99 is the only isotope of technetium in the target. The commercial cyclotrons listed in this thesis have a maximum beam energy of 70 MeV. Thus, proton energies above 70 MeV are not considered for this section.

Table 4.1: Se-79 and total atoms that are irradiated by the proton beam in a selenium target.

| **MeV** | **Penetration (cm)** | **Atoms** (#/$10^{19}$) | **Se-79 Atoms** (#/$10^{19}$) |
|---|---|---|---|
| 18 | 0.075 | 7.6 | 1.1 |
| 23 | 0.159 | 16.0 | 2.3 |
| 30 | 0.304 | 30.7 | 4.4 |
| 50 | 0.862 | 87.0 | 12.3 |
| 70 | 1.617 | 163.0 | 23.1 |

Table 4.2: Zr-93 and total atoms that are irradiated by the proton beam in a zirconium target.

| **MeV** | **Penetration (cm)** | **Atoms** (#/$10^{19}$) | **Zr-93 Atoms** (#/$10^{19}$) |
|---|---|---|---|
| 18 | 0.051 | 6.7 | 1.4 |
| 23 | 0.109 | 14.4 | 2.9 |
| 30 | 0.208 | 27.4 | 5.6 |
| 50 | 0.575 | 75.8 | 15.4 |
| 70 | 1.079 | 142.2 | 28.9 |

Table 4.3: Sn-126 and total atoms that are irradiated by the proton beam in a tin target.

| **MeV** | **Penetration (cm)** | **Atoms** (#/$10^{19}$) | **Sn-126 Atoms** (#/$10^{19}$) |
|---|---|---|---|
| 18 | 0.055 | 5.9 | 1.7 |
| 23 | 0.115 | 12.3 | 3.5 |
| 30 | 0.218 | 23.4 | 6.7 |
| 50 | 0.596 | 64.0 | 18.3 |
| 70 | 1.112 | 119.4 | 34.1 |

As seen above, Tc-99 has the lowest penetration depth out of all of the LLFP materials for any given energy. However, it has the highest number of irradiated atoms due to its high density (11.5 g/cm$^3$) compared to the other materials (see Tables 2.2-2.6) and the fact that it is the only isotope of technetium in the target. This is the opposite case for Cs-135, which

Table 4.4: Cs-135 and total atoms that are irradiated by the proton beam in a CsI compound target.

| **MeV** | **Penetration (cm)** | **Atoms** (#/$10^{19}$) | **Cs-135 Atoms** (#/$10^{19}$) |
|---|---|---|---|
| 18 | 0.081 | 5.2 | 1.0 |
| 23 | 0.175 | 11.3 | 2.1 |
| 30 | 0.327 | 21.2 | 3.9 |
| 50 | 0.916 | 59.3 | 11.0 |
| 70 | 1.715 | 111.0 | 20.6 |

Table 4.5: I-129 and total atoms that are irradiated by the proton beam in a CsI compound target.

| **MeV** | **Penetration (cm)** | **Atoms** (#/$10^{19}$) | **I-129 Atoms** (#/$10^{19}$) |
|---|---|---|---|
| 18 | 0.081 | 5.2 | 1.9 |
| 23 | 0.175 | 11.3 | 4.2 |
| 30 | 0.327 | 21.2 | 7.8 |
| 50 | 0.916 | 59.3 | 21.8 |
| 70 | 1.715 | 111.0 | 40.9 |

Table 4.6: Tc-99 atoms that are irradiated by the proton beam in a technetium target.

| **MeV** | **Penetration (cm)** | **Tc-99 Atoms** (#/$10^{19}$) |
|---|---|---|
| 18 | 0.030 | 6.6 |
| 23 | 0.063 | 13.9 |
| 30 | 0.119 | 26.2 |
| 50 | 0.333 | 73.3 |
| 70 | 0.613 | 134.8 |

is contained within a CsI compound. The largest penetration depth can be seen in the CsI compound, which has the lowest density of all of the elemental LLFP materials. The low density and the number of other cesium and iodine isotopes existing within the compound contribute to the fact that Cs-135 has the least number of atoms irradiated. The maximum penetration depths are used as the length of the targets in the next sub-sections of this thesis, while the number of irradiated atoms are used to find the initial starting mass of the target before undergoing depletion. The non-LLFP isotopes found in each elemental material will affect the depletion of the LLFP isotopes, as they will both compete for transmutation inside the target. Isotope separation will not be considered for this thesis. The penetration depth of the proton beam in the target is proportional to the energy of the beam for all of the LLFP materials. As the beam energy increases, more nuclides are irradiated, making higher beam energies more likely to result in increased transmutation rates.

### 4.1.3 Flux Spectrum Analysis

PHITS is used to find the proton and neutron flux spectra of the targets undergoing proton irradiation. The targets are set with a length equivalent to the maximum penetration depth of the proton beam inside the elemental LLFP material. Each target again exposed to proton beams of 18, 23, 30, 50, and 70 MeV, and the proton and neutron spectra are obtained for each case in a 162-energy group. However, the energy spectrum is cut to a 70-energy group representation as the rest of the upper energy groups are greater than 70 MeV. Figures 4.3-4.7 below show the flux-energy spectrum for elemental selenium targets at differing beam energies. The flux-energy spectra for the other materials can be found in the appendix.

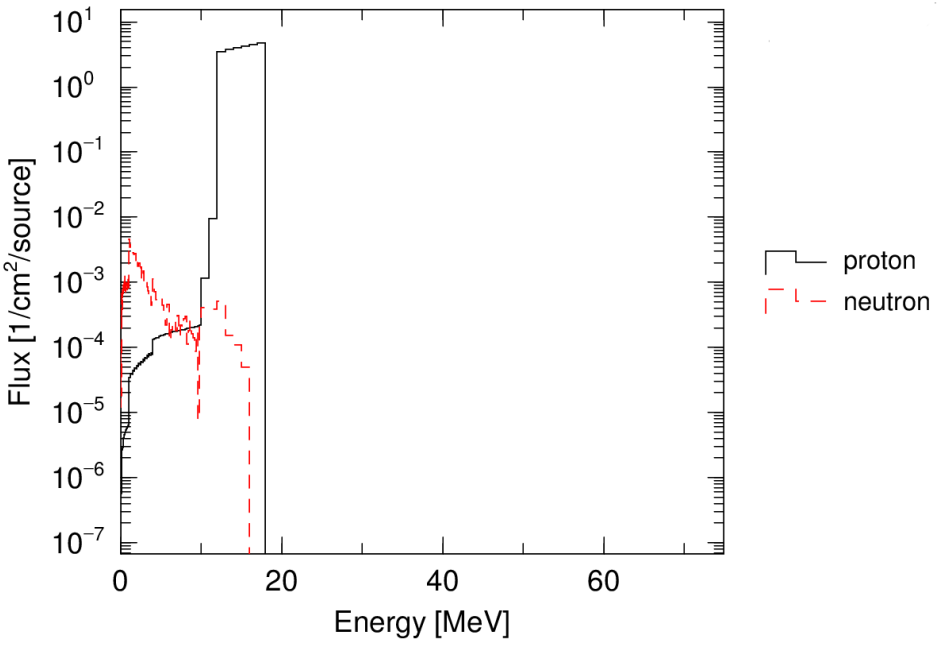


Figure 4.3: Flux per source energy spectrum analysis inside an elemental selenium target with an 18 MeV proton beam.

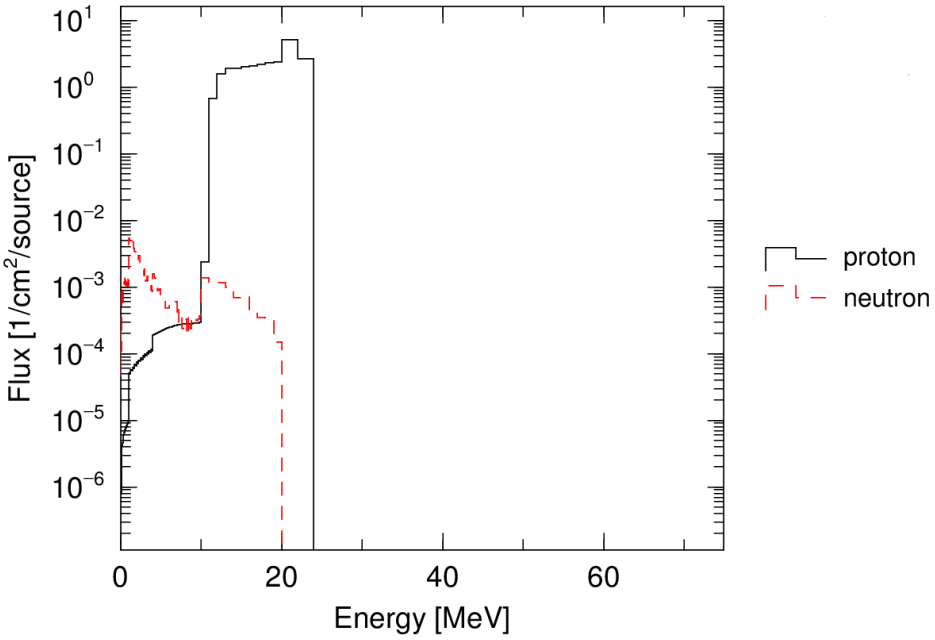


Figure 4.4: Flux per source energy spectrum analysis inside an elemental selenium target with an 23 MeV proton beam.

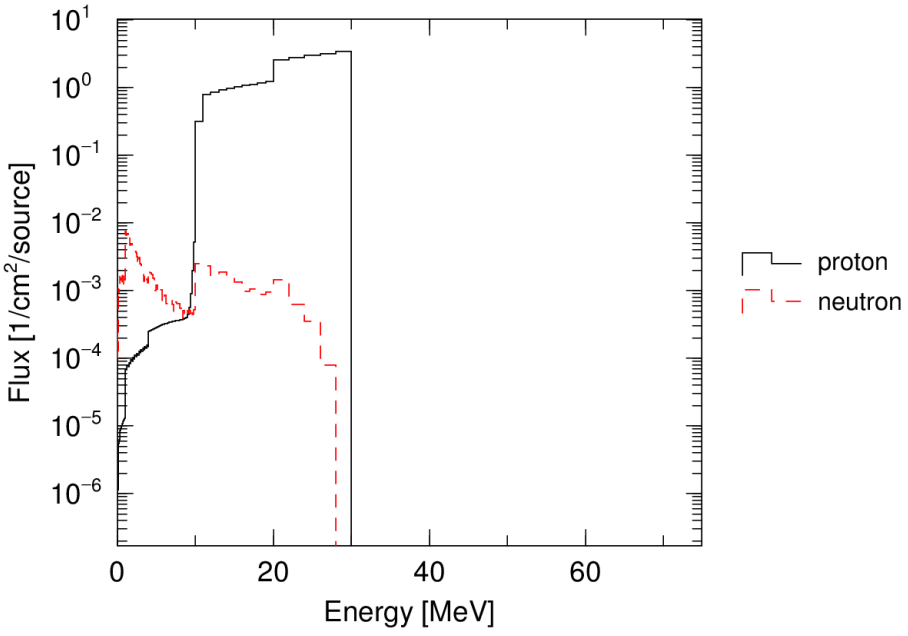


Figure 4.5: Flux per source energy spectrum analysis inside an elemental selenium target with an 30 MeV proton beam.

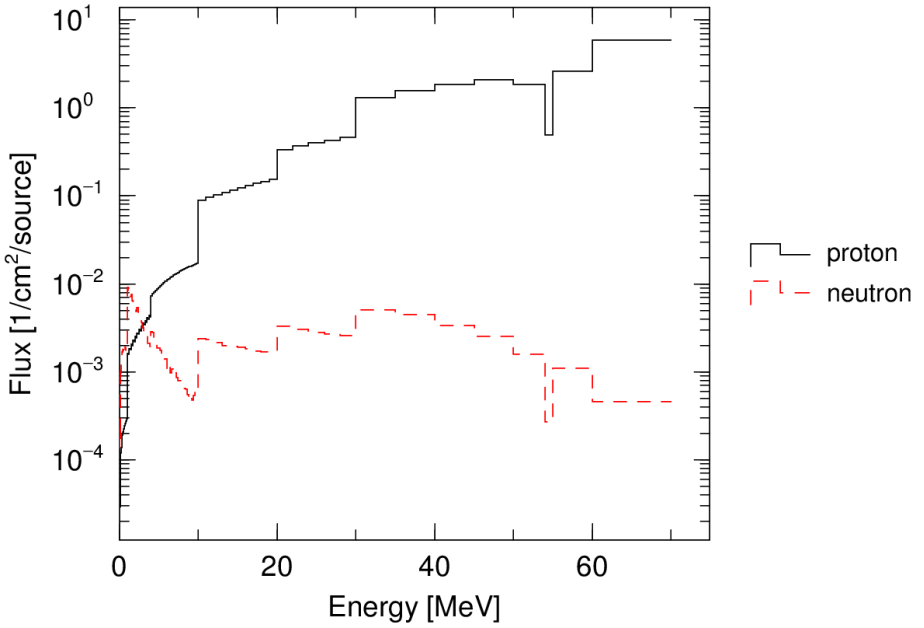


Figure 4.6: Flux per source energy spectrum analysis inside an elemental selenium target with an 50 MeV proton beam.

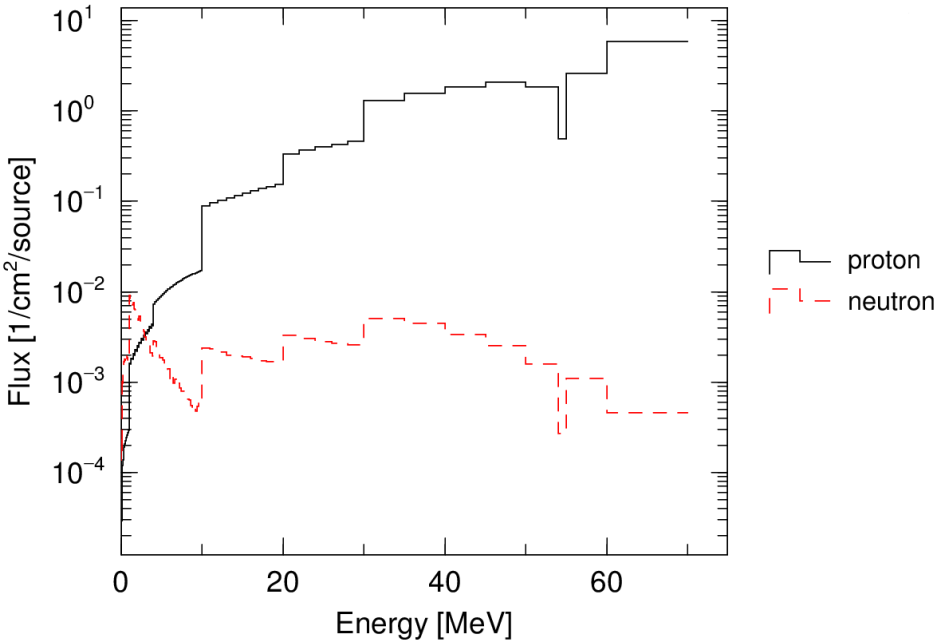


Figure 4.7: Flux per source energy spectrum analysis inside an elemental selenium target with an 70 MeV proton beam.

Note that the flux is listed in units of $1/(\text{cm}^2/\text{source})$, where the source refers to the normalization factor attributed to the 10 mA beam current. The normalization factor is not applied for the figures above. For use in FISPACT, the normalization factor is applied to the flux-energy spectrum data. For a 10 mA beam, the normalization factor is found as $6.25 \times 10^{16}$ protons/second, accounting for the fact that the charge of a proton is $1.602 \times 10^{-19}$ coulombs and one ampere is equal to 1 coulomb per second. The flux-energy spectrum data provides information on the characteristics of the proton and neutron fluxes inside the target. As mentioned previously, when the mono-energetic proton beam interacts with the target, it gets attenuated and many protons lose energy. It is noticeable that the neutron flux has an order of magnitude 3-4 times lower than the proton flux. The flux-energy spectrum data and the number of irradiated atoms found previously to calculate the transmutation rate using FISPACT.

### 4.1.4 Depletion Calculations

It is important to find which beam energy results in the optimal transmutation rate for each LLFP isotope. FISPACT was used in a work supporting this thesis to find the decrease of nuclide abundance of the LLFP materials when exposed to the proton beams at the various aforementioned energies [29]. PHITS is also used to compare the transmutation results from FISPACT by using the T-interact tally. Unlike FISPACT, the T-interact tally in PHITS does not require the flux-energy spectrum data and number of atoms irradiated since it solves interactions on the actual geometry in the simulation. In the FISPACT analysis a beam energy of 70 MeV has the highest transmutation rate for all of the LLFP isotopes with the exception of Se-79. Se-79 has the highest transmutation rate when the beam energy is 50 MeV, likely due to its proton interaction cross-sections. Figures 4.8 and 4.9 below show the decrease in nuclide abundance of Se-79 and Zr-93 respectively after 50 hours of irradiation when the elemental targets is exposed to the proton beam. Note that the targets are composed of elemental material, but only the decrease in LLFP nuclei are plotted.

Table 4.7 below showcases the mass of LFFP material transmuted per year for each LLFP isotope using FISPACT. For this analysis, a beam energy of 70 MeV was used for all the simulations except for Se-79, which used 50 MeV. The data provided in this table was provided by the aforementioned companion thesis [29]. PHITS' T-Interact tally was also used to find the transmutation rates per year for each LLFP material when exposed to a proton beam. The transmutation output for the T-Interact tally includes transmutation from absorption and scattering events. Unlike the FISPACT results, the highest transmutation rates for all of the LLFP isotopes were found when exposed to a 70 MeV beam in PHITS for an indefinite period of time. Table 4.8 below shows the transmutation rate in grams per year for each LLFP isotope as well as their starting target mass. Note that the masses denoted as * refer to the starting total elemental mass of the LLFPs.

In both Table 4.7 and Table 4.8, the isotope with the highest transmutation rate in a year is Tc-99, with a rate of 15.401 ± 0.069 g/year and 7.51 ± 1.19 g/year for PHITS and FISPACT respectively. Selenium has the lowest rate of transmutation with a rate of 2.110 ± 0.009 g/year and 0.59 ± 0.12 g/year for PHITS and FISPACT respectively. The differences between the FISPACT and PHITS results can be explained by the physics models and data libraries they each use. The FISPACT analysis uses TALYS-generated

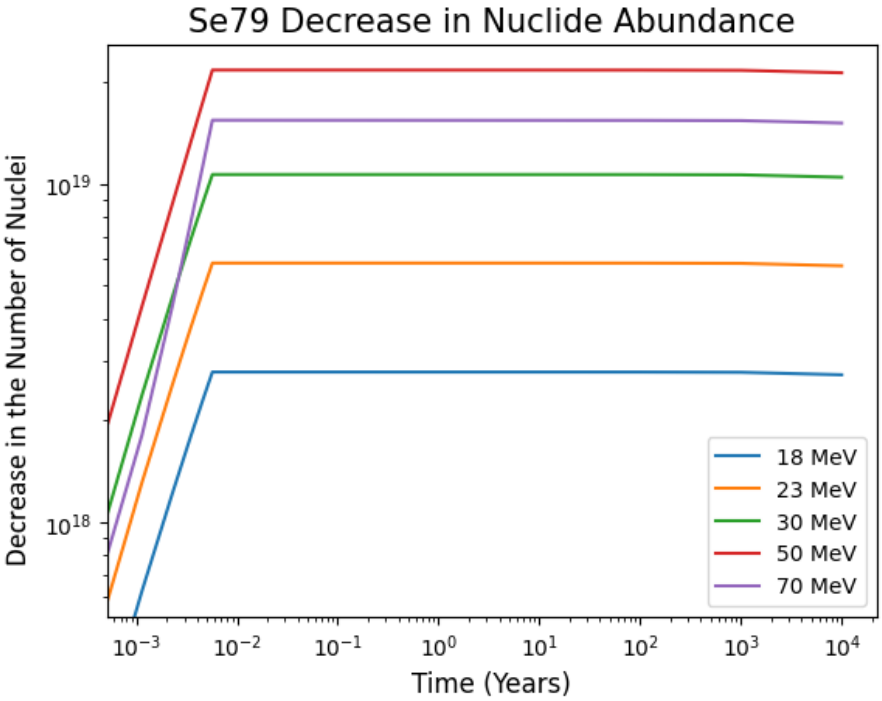


Figure 4.8: Se-79 decrease in nuclide abundance after 50 hours of irradiation adapted from ref [29].

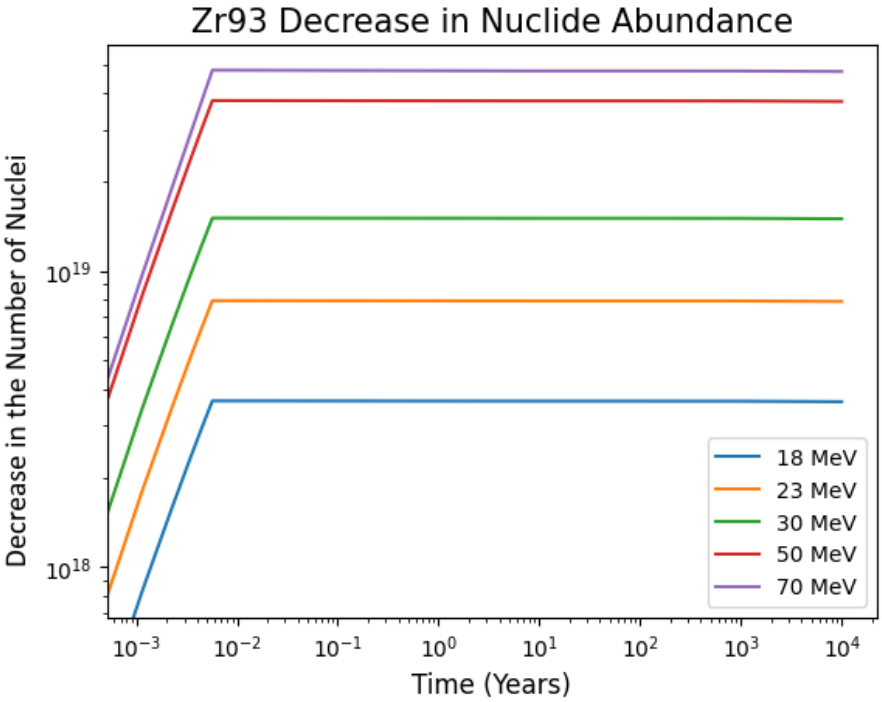


Figure 4.9: Zr-93 decrease in nuclide abundance after 50 hours of irradiation adapted from ref [29].

Table 4.7: Mass and atoms of LLFP material transmuted per year using FISPACT adapted from ref [29].

| **Isotope** | **Transmutation Rate (g/year)** | **Atoms ($\#/10^{19}$)** |
|---|---|---|
| Se-79 | 0.59 ± 0.12 | 2.55 ± 0.53 |
| Zr-93 | 1.31 ± 0.32 | 4.85 ± 1.17 |
| Tc-99 | 7.51 ± 1.19 | 26.1 ± 4.13 |
| Sn-126 | 1.46 ± 0.29 | 3.97 ± 0.78 |
| I-129 | 1.56 ± 0.31 | 4.15 ± 0.85 |
| Cs-135 | 2.02 ± 0.53 | 5.13 ± 1.44 |

Table 4.8: Mass of LLFPs transmuted per year when interacting with a 70 MeV beam using PHITS, the (*) masses refer to the total elemental mass of the LLFPs in the sample.

| **Isotope** | **Transmutation Rate (g/year)** | **Target Mass (g)** |
|---|---|---|
| Se-79(Se) | 2.110 ± 0.009 | 0.031 (0.218*) |
| Zr-93(Zr) | 3.060 ± 0.014 | 0.045 (0.220*) |
| Tc-99(Tc-99) | 15.401 ± 0.069 | 0.221 (0.221*) |
| Sn-126(Sn) | 4.202 ± 0.020 | 0.069 (0.241*) |
| I-129(CsI) | 4.555 ± 0.023 | 0.089 (0.242*) |
| Cs-135(CsI) | 2.403 ± 0.012 | 0.045 (0.242*) |

cross-sections for (p,anything), (p,n), (p,2n), (p,3n), (p,na), (p,np), (p,4n), (p,p), (p,d), (p,t), (p,He3), and (p,a) reaction channels [29]. However, unlike PHITS' INCL model, these reaction channels do not include spallation reactions which can happen above 20 MeV. PHITS also includes neutron interactions when counting transmutation rates. These reasons what likely attributes to the lower estimations of transmutation rates for the FISPACT results compared to the PHITS results.

### 4.1.5 Cost of Transmutation

The transmutation rates of each LLFP isotope as well as the cost per proton for a 70 MeV cyclotron proton beam (as seen in Table 2.9) can be used to find the cost of transmutation. Table 4.9 displays the cost of transmuting one kilogram per year of each LLFP isotope. Note that this only includes the estimated cost for operating the cyclotron beam and the original DOE estimate for power consumption does not include power to grid efficiency.

Tc-99 appears to be the most efficient to transmute per kg when exposed to a 70 MeV beam, costing $82M per kg per year. However, it is also worth considering the production rate of each LLFP material inside a typical PWR. Table 4.10 below showcases the cost of transmutation for each LLFP given the fact that each isotope has a different production rate in a PWR that operates for a year.

Much like Table 4.9, this analysis only accounts for the power costs for running the beam. Accounting for the production rate of each LLFP material in a year from a typical PWR,

Table 4.9: Cost of transmutation per kilogram for a 70 MeV cyclotron with a 10 mA beam current. Note that the transmutation rate is taken from the PHITS depletion analysis and the original DOE estimate for power consumption does not include power to grid efficiency.

| **Isotope** | **Transmutation Rate (kg/year)** | **$ per kg/yr** |
|---|---|---|
| Se-79 | 0.0021 | 605M |
| Zr-93 | 0.0031 | 410M |
| Tc-99 | 0.0154 | 82M |
| Sn-126 | 0.0042 | 302M |
| I-129 | 0.0046 | 276M |
| Cs-135 | 0.0024 | 529M |

Table 4.10: Cost of transmutation per PWR for a 70 MeV cyclotron with a 10 mA beam current. Note that the original DOE estimate for power consumption does not include power to grid efficiency

| **Isotope** | **Production Rate (kg/GW*year) [7]** | **Cost of Transmutation** |
|---|---|---|
| Se-79 | 0.066 | $ 40M |
| Zr-93 | 8.04 | $ 3296M |
| Tc-99 | 8.54 | $ 700M |
| Sn-126 | 0.30 | $ 91M |
| I-129 | 1.96 | $ 541M |
| Cs-135 | 2.76 | $ 1463M |

the LLFPs that are the most feasible to be transmuted appear to be Se-79 and Sn-126. Although Table 4.9 shows that Tc-99 is the cheapest LLFP to transmute per kilogram, a typical PWR produces enough Tc-99 to make its transmutation less viable. Zr-93 and Cs-135 are far less viable for transmutation than the other LLFP isotopes for a 70 MeV cyclotron. If isotopic separation was considered, the cost of transmutation for all of the LLFPs would likely decrease, due to the lack of other competing isotopes inside the target material.

## 4.2 Spallation Analysis

### 4.2.1 Particle Population

As seen in the previous section, transmutation rates of LLFPs from proton beams of energies 18-70 MeV are low compared to the production rates of LLFPs in a typical PWR. Thus, the use of 1000 MeV proton beams will be considered to produce secondary neutrons to be used for transmutation. The first step in producing secondary neutrons is through the spallation process of the highly-energetic proton beam interacting with neutron rich materials. This will create a wide spectrum of neutrons which can then be moderated into the thermal region and be used to transmute LLFP targets around the spallation target. Geant4 is used initially for its ability to individually track all particles that would exist in such a simulation.

This will give clues for what material to use for the spallation target. Tungsten, lead, and Tc-99 were analyzed first for their neutron rich qualities and made into a 1x1x1 $m^3$ cube targets. Ten thousand 1000 MeV protons of a 1 mm radius beam were directed towards each respective target to find the particle population generated by the spallation and secondary processes. Protons and neutrons are individually tracked with the help of Grasshopper, a front-end software developed for Geant4. Table 4.11 below displays Geant4's results for the particles generated per incoming proton for the tungsten, lead, and Tc-99 cube targets. Tc-99 is chosen to be compared to tungsten and lead due to its isotopic purity compared to the other LLFP materials. Table 4.12 below is PHITS' results for the particle population analysis that is used to compare with Table 4.11.

Table 4.11: Particle population of tungsten, lead, and Tc-99 targets generated by the 1000 MeV proton beam spallation process in Geant4.

| **Material** | **Neutrons per Incoming Proton** | **Protons per Incoming Proton** |
|---|---|---|
| Tungsten | 43.152 | 3.794 |
| Lead | 43.127 | 3.570 |
| Tc -99 | 29.576 | 5.633 |

Table 4.12: Particle population of tungsten, lead, and Tc-99 targets generated by the 1000 MeV proton beam spallation process in PHITS.

| **Material** | **Neutrons per Incoming Proton** | **Protons per Incoming Proton** |
|---|---|---|
| Tungsten | 33.381 | 5.703 |
| Lead | 33.205 | 5.432 |
| Tc-99 | 23.080 | 7.334 |

PHITS uses the INCL 4.6 and Evaporation (GEM) models for neutron and protons, while Geant4 uses the INCL++ model which are both similar in function. Results for both PHITS and Geant4 are similar but with slight differences, with the neutron per incident proton ratio for PHITS being lower than Geant4's results by around 25-30%. The generated proton per incident proton is higher for PHITS than it is for Geant4 by around 30-50%. Despite this, both tool-kits indicate similar trends: tungsten and lead produce more neutrons than Tc-99, while Tc-99 generates a higher number of protons. In Table 4.13 below, PHITS was used to find the particle population of the elemental LLFP materials in the aforementioned 1x1x1 $m^3$ cube target configuration to find how Tc-99 compares to the other LLFP materials as a spallation target.

As seen in Table 4.13, Tc-99 produced the highest number of protons when interacting with the spallation proton beam, while tin produced the highest number of neutrons. However, this preliminary analysis involves the use of a 1x1x1 $m^3$ cube as the spallation targets, and the secondary neutrons that are produced as a result would be localized within the target itself. The spallation target should be smaller in size to allow the secondary neutrons to escape the spallation target and reach their intended transmutation targets.

Table 4.13: Particle population of elemental LLFP materials generated by the 1000 MeV proton beam spallation process in PHITS.

| Material | Neutrons per Incoming Proton | Protons per Incoming Proton |
|---|---|---|
| Selenium | 19.283 | 6.235 |
| Tc-99 | 23.080 | 7.334 |
| Zirconium | 22.262 | 6.531 |
| Tin | 31.001 | 5.109 |
| CsI | 23.581 | 5.268 |

### 4.2.2 Spallation Target Design

Before finding the best candidate for the spallation target, the maximum penetration depth for each material is analyzed. Following the analysis on the 1x1x1 $m^3$ cube spallation target, the preliminary testing analyzes cylindrical targets. Each target is a long cylindrical object with a radius of 2.0 cm and 150 cm long. To find the penetration depth of the proton beam in the target, the targets undergo exposure to 1000 MeV proton beams in PHITS in a 1.0 cm radius, while recording the distances traveled by the protons within the targets. Figure 4.10 below showcases the proton penetration depth in an elemental selenium target with a radius of 2.0 cm and beam radius of 1.0 cm at 1000 MeV.

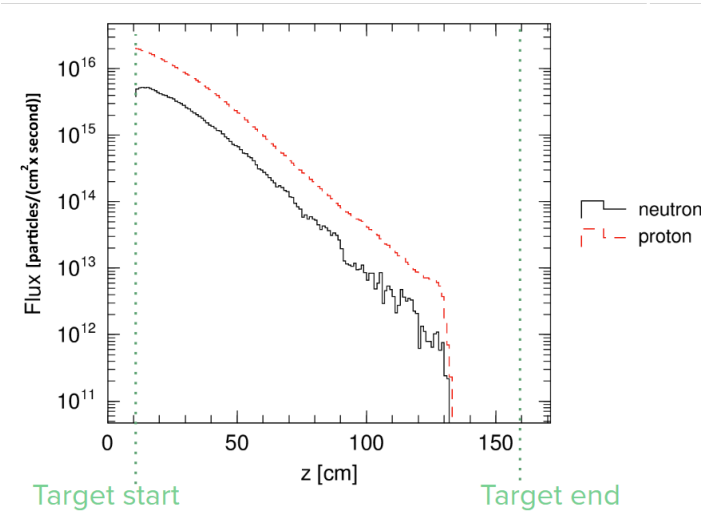


Figure 4.10: 1.0 cm radius proton beam penetration depth in a 2.0 cm radius elemental selenium target at 1000 MeV. Note that the source value of $6.25 \times 10^{16}$ protons/second attributed to a 10 mA beam is multiplied to the results.

For the spallation case the penetration depth is determined on the z-axis as the point where the proton flux diminishes by 3 orders of magnitude compared to the magnitude of the initial incoming proton flux. For all of the tested materials, this point is close to the point where the proton flux drops to zero, as can be seen in Figure 4.10 above. Table 4.14 below displays the penetration depth and total number of irradiated atoms for each material.

Table 4.14: Penetration depth and total number of atoms irradiated for each material where the target radius is 2.0 cm and the beam radius is 1.0 cm.

| Material | Penetration Depth (cm) | Total Irradiated Atoms |
|---|---|---|
| Selenium | 119 | 4.80E+25 |
| Tc-99 | 45 | 3.96E+25 |
| Zirconium | 80 | 3.94E+25 |
| Tin | 81 | 2.92E+25 |
| CsI | 122 | 2.87E+25 |
| Lead | 55 | 2.28E+25 |

To find the best candidate material for the spallation target, the average proton and neutron fluxes are analyzed on the outer surface areas of each material at radii of 1.0 cm and 2.0 cm. Each material target has a radius of 2.0 cm and length equal to the maximum penetration depth of that material. The best candidate will maximize the number of secondary neutrons produced, thus having the highest neutron flux. Table 4.15 below shows the proton and neutron fluxes for each material at radii of 1.0 cm and 2.0 cm.

Table 4.15: Proton and neutron fluxes at outer surface area for a 1.0 cm radius beam and 2.0 cm target. Note that the surface flux is found at both R=1.0 cm and R=2.0 cm.

| Material | Proton Flux (1 cm) | Neutron Flux (1 cm) | Proton Flux (2 cm) | Neutron Flux (2 cm) |
|---|---|---|---|---|
| Selenium | $1.99 \times 10^{15}$ | $8.94 \times 10^{14}$ | $2.08 \times 10^{14}$ | $4.44 \times 10^{14}$ |
| Tc-99 | $2.59 \times 10^{15}$ | $2.93 \times 10^{15}$ | $2.02 \times 10^{14}$ | $1.33 \times 10^{15}$ |
| Zirconium | $2.27 \times 10^{15}$ | $1.49 \times 10^{15}$ | $2.22 \times 10^{14}$ | $7.16 \times 10^{14}$ |
| Tin | $2.21 \times 10^{15}$ | $1.86 \times 10^{15}$ | $2.21 \times 10^{14}$ | $9.06 \times 10^{14}$ |
| CsI | $1.98 \times 10^{15}$ | $1.07 \times 10^{15}$ | $2.32 \times 10^{14}$ | $5.43 \times 10^{14}$ |
| Lead | $2.46 \times 10^{15}$ | $3.82 \times 10^{15}$ | $2.22 \times 10^{14}$ | $1.81 \times 10^{15}$ |

From these results it is apparent that lead performs better as a spallation target, however Tc-99 does surprisingly well as well. Out of the LLFP materials, Tc-99 shows the most promise in utilizing the proton flux to produce secondary neutrons, having the highest neutron flux and the lowest proton flux at a radius of 2.0 cm. In comparison to lead, there is around a 25% decrease in the outgoing neutron flux for Tc-99. However, Tc-99 will be actively transmuted by the spallation reactions caused by the 1000 MeV proton beam. There is still a considerably high proton flux leaving the selenium region outer surface areas. This suggests that the proton flux is not being completely utilized to produce secondary neutrons.

The spallation target will need to have a larger radius to fully utilize the proton flux and potentially increase the transmutation rate. A preliminary test was designed to find the approximate desired radius of a Tc-99 target. The desired target radius is defined as the point where the incoming proton flux is utilized to create many secondary neutrons, while keeping the target small enough to lower the chances of the neutron absorption inside the target. The secondary neutrons can be used to transmute LLFP material around the spallation target, which is discussed in the next section. A 6.0 cm radius Tc-99 target is divided into two separate sections where the proton and neutron transmutations are analyzed for each

section. Figure 4.11 below displays the transmutations per source in 1 $cm^3$ for a 5.0 cm radius Tc-99 target (left) and a 1.0 cm thick Tc-99 section (right) that surrounds the target.

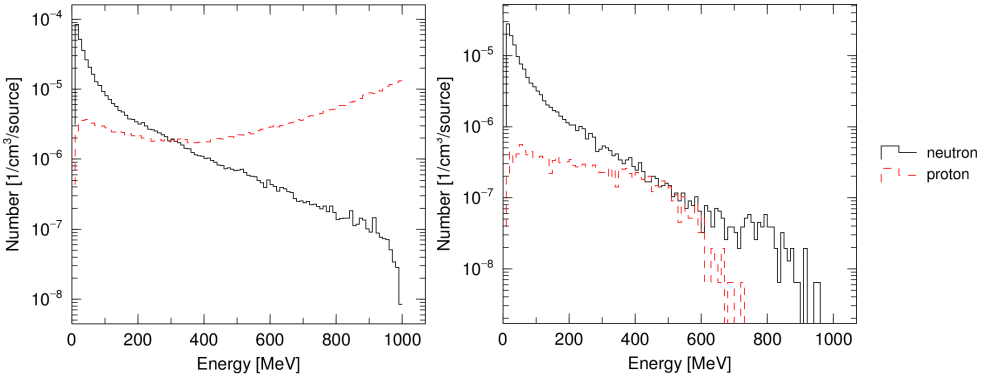


Figure 4.11: Transmutations per source in 1 $cm^3$ for a 5.0 cm radius Tc-99 target (left) and the 5.0-6.0 cm outer radius Tc-99 section (right) when interacting with a 1000 MeV beam.

Accounting for volume, the average transmutations per source for the 5.0 cm inner radius target are 1.3696 ± 0.0062 and 1.3619 ± 0.0045 for protons and neutrons respectively. For the 1.0 cm thick 5.0-6.0 cm outer radius Tc-99 section, the average transmutations per source are 0.0227 ± 0.0005 for protons and 0.2080 ± 0.0016 for neutrons. Thus, the 5.0 cm inner radius Tc-99 target uses the proton flux to create secondary neutrons as much as possible without absorbing as much of the neutron flux that a larger target would do. Both Tc-99 and lead will be used as spallation targets for the next section and compared for their ability to create secondary neutrons that will be used to transmute LLFP material.

### 4.2.3 Tank Design with LLFP pins

A large tank design has been developed to maximize the transmutation rate as much as possible from the secondary neutrons. Figures 4.12 and 4.13 below showcase the tank design in the X-Y and X-Z plane views respectively. For this case, the beam characteristics remain the same with a beam energy of 1000 MeV, beam current of 10 mA, and a radius of 1.0 cm. The 5.0 cm radius and 200 cm long spallation target (pictured in pink) is in the middle of the tank, which contains a 1.0 cm radius and 100 cm long void region.

This void region ensures that the proton spallation beam interacts with the spallation target in the center of the tank. There are 1782 1.0 cm radius and 200 cm long cylindrical pins that surround the spallation target, which are composed of LLFP material. The LLFP pins are surrounded by heavy water (pictured in brown) and a 20 cm thick beryllium reflector surrounds the tank on all sides (pictured in blue). Heavy water is classified as a form of water where the hydrogen atoms are composed of deuterium instead of hydrogen-1. Heavy water was chosen for its ability to thermalize fast neutrons and its low neutron absorption cross-section compared to light water [30]. This allows the secondary neutrons that leave the spallation target to slow down with low neutron loss, greatly increasing the chances of interaction between the neutrons and the LLFP pins. Beryllium is used to surround the tank because of its good reflective properties and the fact that it has the lowest neutron

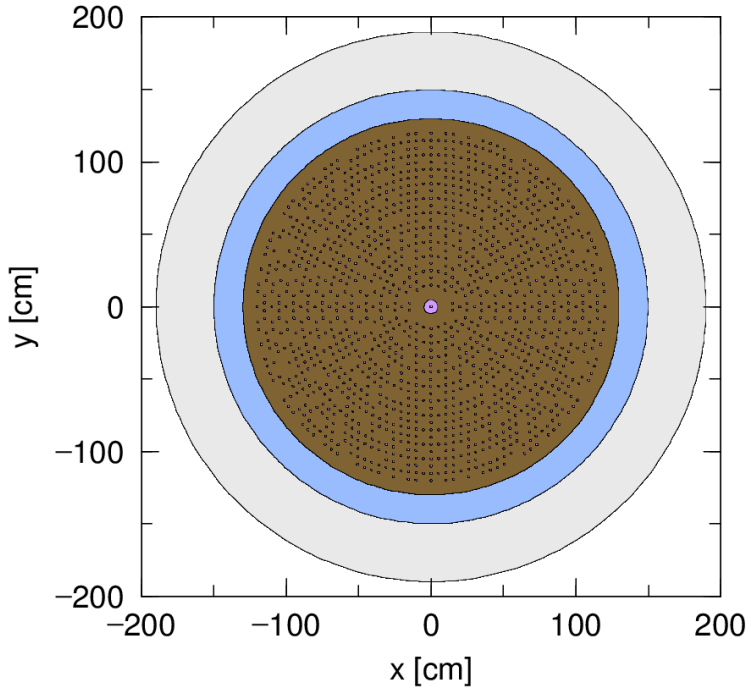


Figure 4.12: Tank design with LLFP pins surrounded by heavy water and a beryllium reflector from an X-Y plane view.

absorption cross-section out of all the metals. Beryllium also has a high (n,2n) reaction cross-section, where neutron collisions will create neutrons that may redirect back into the system [31]. As mentioned before, the spallation target will be composed of Tc-99 or lead. These two materials will be compared for their abilities to deplete the LLFP regions from the secondary neutrons that are created from the spallation process.

### 4.2.4 Depletion Calculations

The added benefit of using Tc-99 instead of lead for the spallation target is the fact that the spallation process itself will transmute nuclides of Tc-99. PHITS is used to calculate the depletion rate of the spallation target when it is composed of Tc-99, using the T-Interact tally. PHITS uses the INCL library in this simulation and includes spallation reactions in the depletion tally. Table 4.16 below exhibits the transmutation rate of the Tc-99 spallation target induced from protons and neutrons.

In Tables 4.17 and 4.18 below, FISPACT is used to calculate the transmutation rate in the LLFP pins from non-spallation neutron reactions.

FISPACT is used for the LLFP region depletion analysis because of the lack of thermalized neutron analysis in the PHITS INCL model. Similarly to the 70 MeV analysis, the neutron energy-flux spectrum and target mass were obtained from the PHITS simulations to find the depletion rate in FISPACT. The neutron energy-flux spectra can be found in the Appendix. The Irradiation was performed performed for 50 hours and the amount of mass transmuted post-irradiation for a year was used to calculate the transmutation rates.

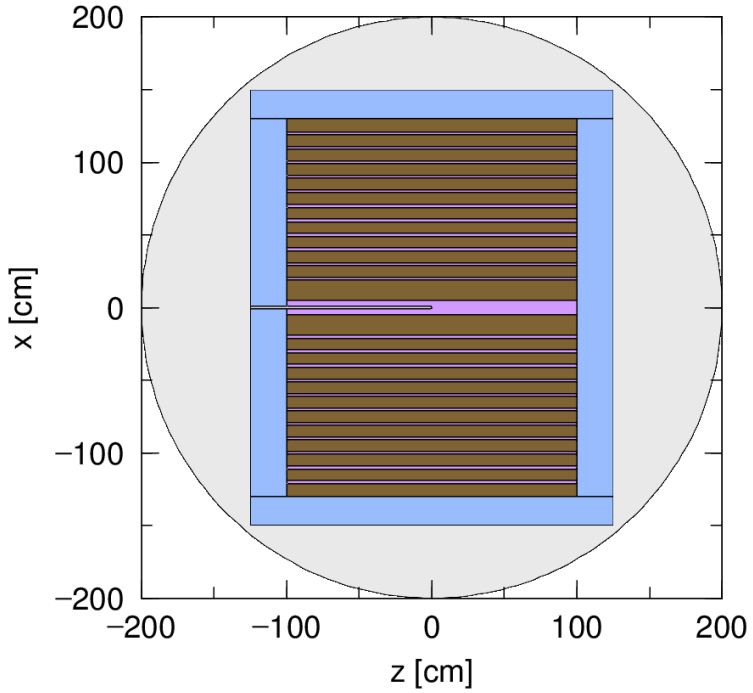


Figure 4.13: Tank design with LLFP pins surrounded by heavy water and a beryllium reflector from an X-Z plane view.

Table 4.16: Transmutation rates of the Tc-99 spallation target using PHITS.

| **Tc-99 Spallation Target** | |
|---|---|
| Proton Induced Transmutation (kg/year) | 0.440 ± 0.002 |
| Neutron Induced Transmutation (kg/year) | 0.453 ± 0.001 |
| Total Transmutation (kg/year) | 0.893 ± 0.002 |
| Target Mass (kg) | 177.03 |

Table 4.17: Mass of LLFPs inside the tank configuration transmuted per year when interacting with a secondary neutrons generated from a Tc-99 target, the (*) masses refer to the total elemental mass of the LLFPs in the sample.

| **Isotope** | **Transmutation Rate (kg/year)** | **LLFP Pin Mass (kg)** |
|---|---|---|
| Se-79(Se) | 1.1 | 683 (4815*) |
| Zr-93(Zr) | 1.0 | 1481 (7278*) |
| Tc-99(Tc-99) | 10.9 | 12876 (12876*) |
| Sn-126(Sn) | 4.0 | 2206 (7726*) |
| I-129(CsI) | 1.0 | 1859 (5038*) |
| Cs-135(CsI) | 0.7 | 937(5038*) |

Although Table 4.16 above shows almost of kilogram of Tc-99 can be transmuted directly from the spallation process, Tables 4.17 and 4.18 show that there is a performance penalty

Table 4.18: Mass of LLFPs inside the tank configuration transmuted per year when interacting with a secondary neutrons generated from a lead target.

| **Isotope** | **Transmutation Rate (kg/year)** | **LLFP Pin Mass (kg)** |
|---|---|---|
| Se-79(Se) | 2.1 | 683 (4815*) |
| Zr-93(Zr) | 6.2 | 1481 (7278*) |
| Tc-99(Tc-99) | 20.0 | 12876 (12876*) |
| Sn-126(Sn) | 8.0 | 2206 (7726*) |
| I-129(CsI) | 3.0 | 1859 (5038*) |
| Cs-135(CsI) | 1.3 | 937(5038*) |

in transmutation for the LLFP region when using Tc-99 as a spallation target instead of lead. The transmutation rates in the LLFP pins approximately double when using lead as a spallation target, except for Zr-93, which increases more than sixfold. For both spallation target options, Tc-99 and Sn-126 have the highest transmutation rates, while Cs-135 has the lowest. Although Tc-99 transmutation rates are high when using lead as a spallation target, only around 0.155% of the original Tc-99 LLFP pin mass is transmuted every year. Transmutation rates appear to be dependent on the mass of LLFP material inside the pins. A higher mass present in pins of a constant volume will generally lead to higher transmutation rates. However, some LLFPs may transmute better than others due to the differences in neutron reaction cross-sections. For example, figures 4.14 and 4.15 below display total, elastic and inelastic scattering, and capture neutron cross-sections for Tc-99 and Cs-135 from PHITS' JENDL-4.0 data library.

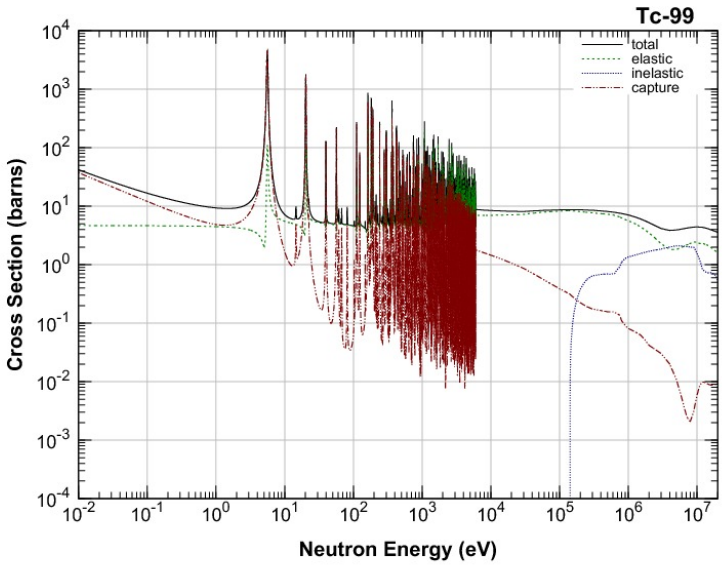


Figure 4.14: Total, elastic and inelastic scattering, and capture neutron cross sections for Tc-99 adapted from ref [32].

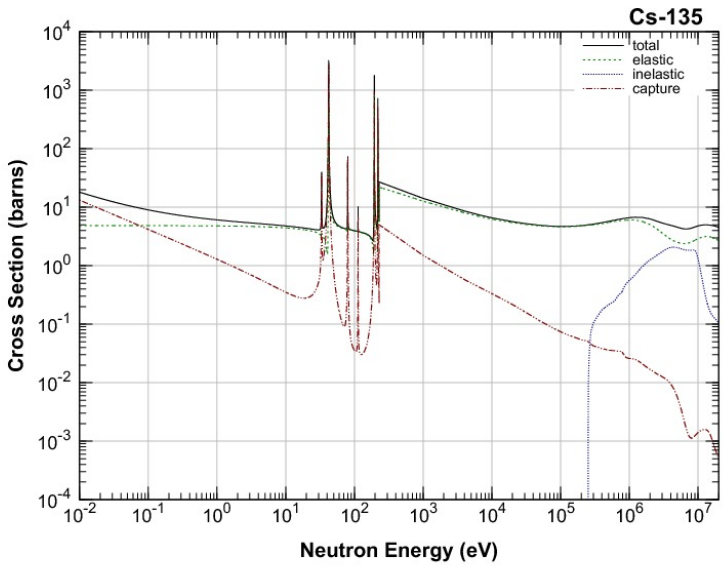


Figure 4.15: Total, elastic and inelastic scattering, and capture neutron cross sections for Cs-135 adapted from ref [32].

Future analysis of the tank design with LLFP pins will involve using different numbers of LLFP pins, changing the size and material of the spallation target, and experimenting with different moderator and reflector materials.

### 4.2.5 Cost of Transmutation

The transmutation rates of each isotope and the cost per proton for a 1000 MeV beam are used to find the cost of transmutation for each material. Tables 4.19 and 4.20 showcase the cost of transmuting one kilogram per year of each LLFP isotope for Tc-99 and lead spallation targets respectively.

Table 4.19: Cost of transmutation per kilogram for a 1000 MeV accelerator with a Tc-99 spallation target. Note that a power to grid beam efficiency of 13% is considered for power consumption requirements.

| **Isotope** | **Transmutation Rate (kg/year)** | **$ per kg/yr** |
|---|---|---|
| Se-79 | 1.1 | 11M |
| Zr-93 | 1.0 | 12M |
| Tc-99 | 10.9 | 1.1M |
| Sn-126 | 4.0 | 3M |
| I-129 | 1.0 | 12M |
| Cs-135 | 0.7 | 17M |

Table 4.20: Cost of transmutation per kilogram for a 1000 MeV accelerator with a lead spallation target. Note that a power to grid beam efficiency of 13% is considered for power consumption requirements.

| Isotope | Transmutation Rate (kg/year) | $ per kg/yr |
|---|---|---|
| Se-79 | 2.1 | 5.7M |
| Zr-93 | 6.2 | 1.9M |
| Tc-99 | 20.0 | 0.6M |
| Sn-126 | 8.0 | 1.5M |
| I-129 | 3.0 | 4M |
| Cs-135 | 1.3 | 9.2M |

For each kilogram, Tc-99 is the most efficient LLFP to transmute when exposed to a 1000 MeV beam, costing $3M and $0.6M when using Tc-99 and lead spallation targets respectively. Table 4.21 below showcases the cost of transmutation for each LLFP given the fact that each isotope has a different production rate in a PWR that operates for a year. Both of the results for the lead and Tc-99 spallation target configurations are considered below.

Table 4.21: Cost of transmutation per PWR for each spallation target design. Note that a power to grid beam efficiency of 13% is considered for power consumption requirements.

| Isotope | Production Rate (kg/GW*year) [7] | Tc-99 | Lead |
|---|---|---|---|
| Se-79 | 0.066 | $ 0.7M | $ 0.4M |
| Zr-93 | 8.04 | $ 96.5M | $ 15.3M |
| Tc-99 | 8.54 | $ 9.4M | $ 5.1M |
| Sn-126 | 0.30 | $ 0.9M | $ 0.5M |
| I-129 | 1.96 | $ 23.5M | $ 7.8M |
| Cs-135 | 2.76 | $ 46.9M | $ 25.3M |

Lead used as a target significantly reduces the costs per transmutation while accounting for production rates compared to using Tc-99 as a target. Compared to Table 4.9, the cost of transmutation per PWR is significantly more cost effective for both the lead and Tc-99 designs. The most expensive option for transmutation is Zr-93 when using the Tc-99 target. However, it becomes more cost effective to transmute compared to Cs-135 when lead is used as a target. Much like Table 4.9 above, Se-79 and Sn-126 are the most feasible LLFPs to transmute from spent fuel. Further analysis into target designs and isotopic separation can potentially further decrease the transmutation costs for all of the LLFP isotopes.

# Chapter 5

# Conclusions and Future Work

## 5.1 Conclusions

This thesis explores the feasibility of using cyclotrons at beam energies of 18-70 MeV and 1000 MeV spallation proton sources for LLFP transmutation, with a focus on optimizing material configuration designs to maximize transmutation efficiency. The transmutation analyses for both the cyclotron at beam energies of 18-70 MeV and the spallation cases show improvement over the control. However, the 70 MeV cyclotron case is less promising than the spallation case, with the highest transmutation rate recorded at 15.401 $\pm$ 0.069 g/year for a Tc-99 target. This would require \$82M worth of power to transmute a single kilogram of Tc-99 assuming the use of a 10 mA beam and commercial electricity costs in Massachusetts in 2024. Each LLFP gets produced at differing rates in a single year in a typical 1 GW PWR. Although Se-79 is typically produced at a rate 66 g/year, the transmutation rate is only 2.110 $\pm$ 0.009 g/year for this design. At least 32 cyclotrons with beam energies of 10 mA would be required to fully transmute 66 grams a year of Se-79, totaling \$40M of expenses for just the beam costs.

Transmutation rates are significantly increased when utilizing secondary neutrons generated from the 1000 MeV proton beam interacting with the spallation target in the tank design with LLFP pins. When Tc-99 is used as a spallation target in the tank design, the spallation reactions directly deplete 0.893 $\pm$ 0.002 kg/year of Tc-99. Additionally, the Tc-99 target transmutes approximately 10.9 kg/year of Tc-99 in the LLFP pins through secondary neutrons generated by the spallation process. Combined with the direct depletion from spallation reactions, this results in a total transmutation rate of 11.8 kg/year of Tc-99 across both the LLFP regions and the target. Although using lead as a spallation target does not have the benefit of directly transmuting an LLFP material through spallation reactions, it significantly increases the transmutation rate in the LLFP regions, achieving approximately 20.0 kg/year of Tc-99 transmuted in the LLFP pins. This translates to a transmutation cost of \$1.1M per kg and \$0.6M per kg for Tc-99 when using Tc-99 and lead targets, respectively. The most efficient LLFP to transmute when using either the lead or Tc-99 target is Se-79 when accounting for the production rates of LLFPs in a 1GW PWR. Transmuting 66 grams of Se-79 in the tank design requires \$0.7M and \$0.4M worth of beam cost expenses for Tc-99 and lead targets respectively.

Transmutation can be further enhanced through several approaches. Increasing the beam energy can augment the number of atoms irradiated in a target. A higher number of irradiated atoms in more nuclides having the opportunity to transmute. The proton beam flux can be further increased if a higher beam current is sustainable, further contributing to the transmutation rate. Additionally, using other neutron-rich materials as the spallation target can increase the number of secondary neutrons generated during the spallation process.

## 5.2 Future Work

Future work will involve testing additional materials and design configurations to optimize the LLFP transmutation rate. Given the higher transmutations rates attributed to the spallation process compared to the 70 MeV cyclotron case, it is likely to be the preferred method in future iterations. Different materials will be tested as moderators or reflectors to assess their impact on the energy-flux spectrum of secondary neutrons within the design configuration. To better understand how transmutation outcomes are influenced by design sensitivities, several parameters will be analyzed. These include the total mass of LLFPs, the material and size of the spallation target, the number and size of LLFP pins, and the inclusion of cladding around the LLFP pins. Analyzing the secondary neutron spectrum will provide insight into which neutrons contribute most to LLFP transmutation. Since thermal and fast neutrons interact differently with each isotope, varying levels of neutron moderation may be needed to fully optimize transmutation for each material.

This thesis uses beam energies that are soon sustainable with current cyclotron and accelerator beam powers. Future work will also explore the use of higher beam energies and different beam powers. While this thesis considers only one beam at a time, the potential use of multiple beam-lines could be explored to achieve faster transmutation rates. Although the heat deposited onto the targets was not considered in this thesis, it is crucial for future investigation. Materials capable of withstanding high heat deposition or facilitating cooling are currently under review. Additionally, understanding the energy requirements and costs associated with cooling the system is essential to fully evaluate the feasibility of each design.

# Appendix A

# PHITS

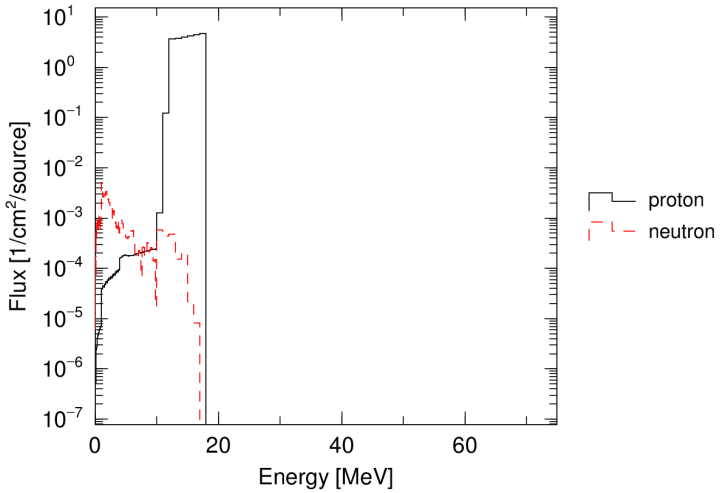


Figure A.1: Flux per source energy spectrum analysis inside an elemental zirconium target with an 18 MeV proton beam.

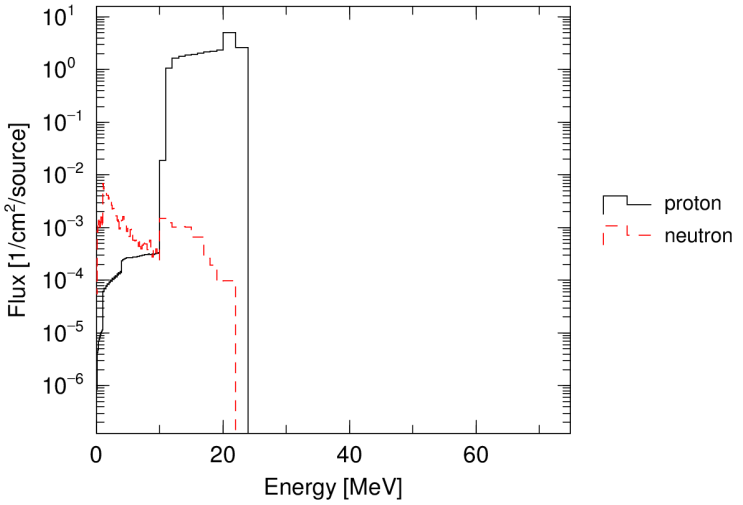


Figure A.2: Flux per source energy spectrum analysis inside an elemental zirconium target with an 23 MeV proton beam.

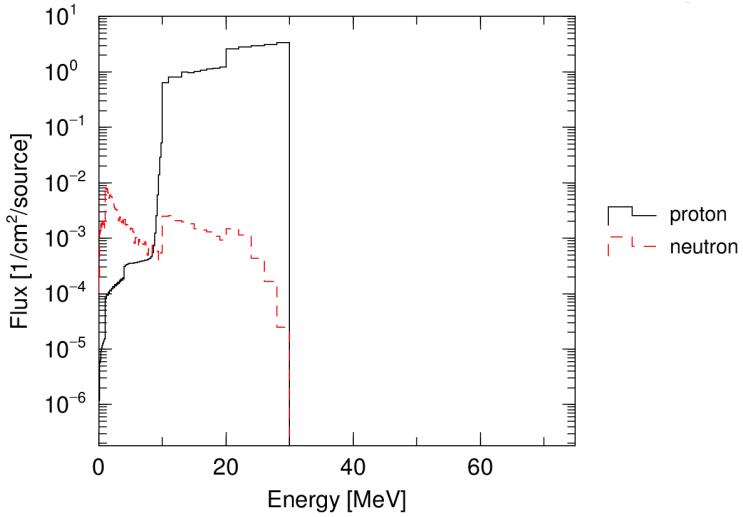


Figure A.3: Flux per source energy spectrum analysis inside an elemental zirconium target with an 30 MeV proton beam.

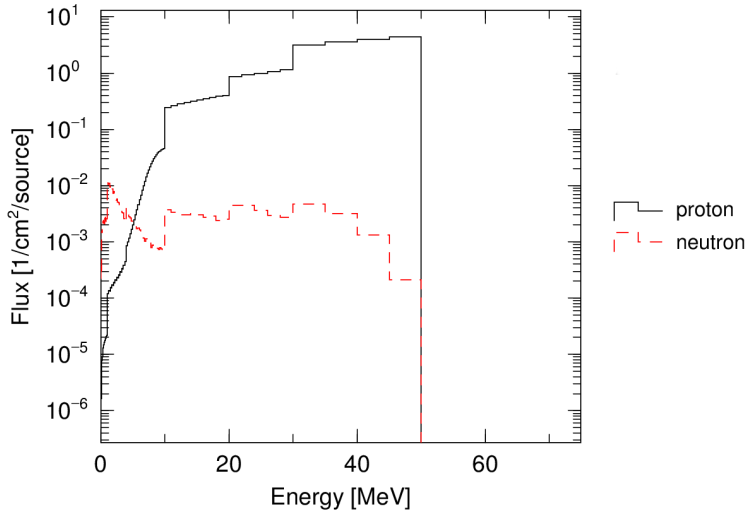


Figure A.4: Flux per source energy spectrum analysis inside an elemental zirconium target with an 50 MeV proton beam.

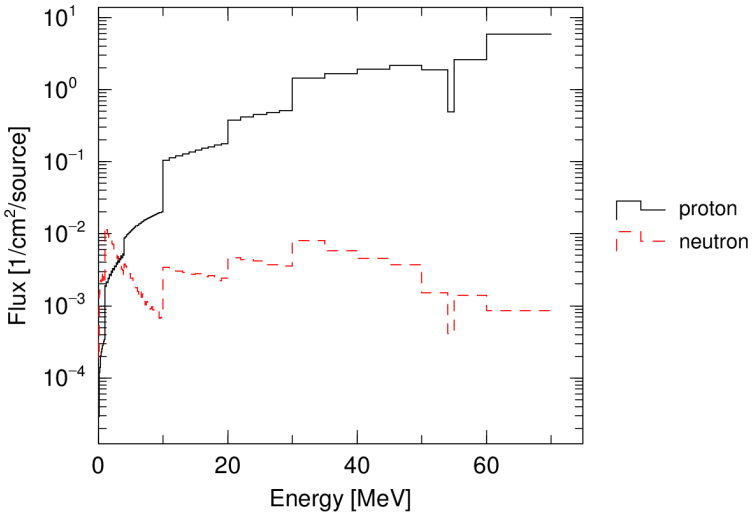


Figure A.5: Flux per source energy spectrum analysis inside an elemental zirconium target with an 70 MeV proton beam.

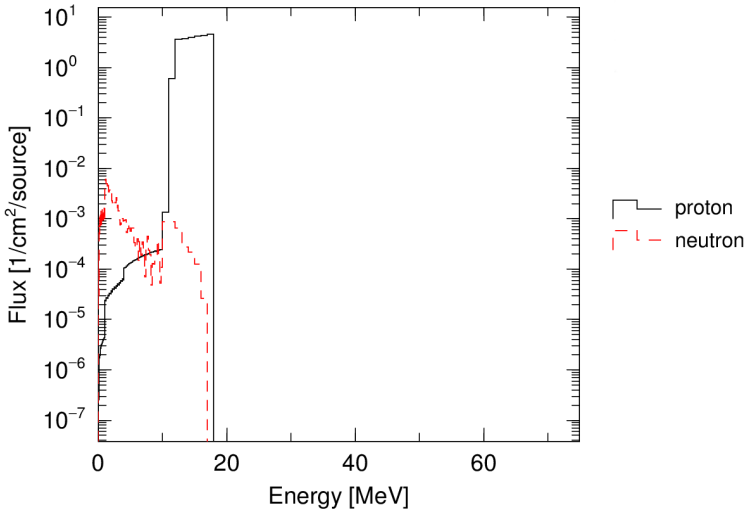


Figure A.6: Flux per source energy spectrum analysis inside a Tc-99 target with an 18 MeV proton beam.

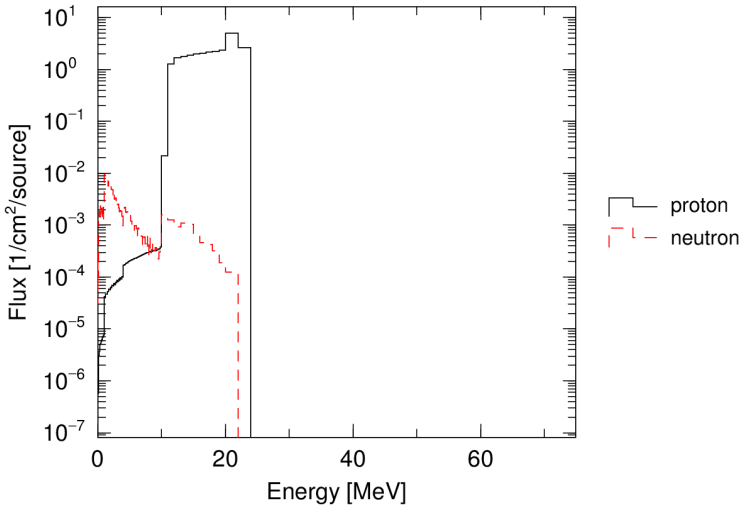


Figure A.7: Flux per source energy spectrum analysis inside a Tc-99 target with an 23 MeV proton beam.

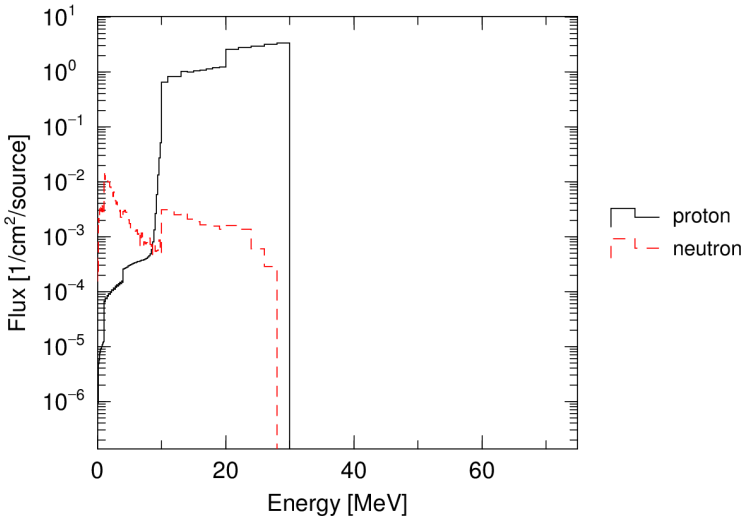


Figure A.8: Flux per source energy spectrum analysis inside a Tc-99 target with an 30 MeV proton beam.

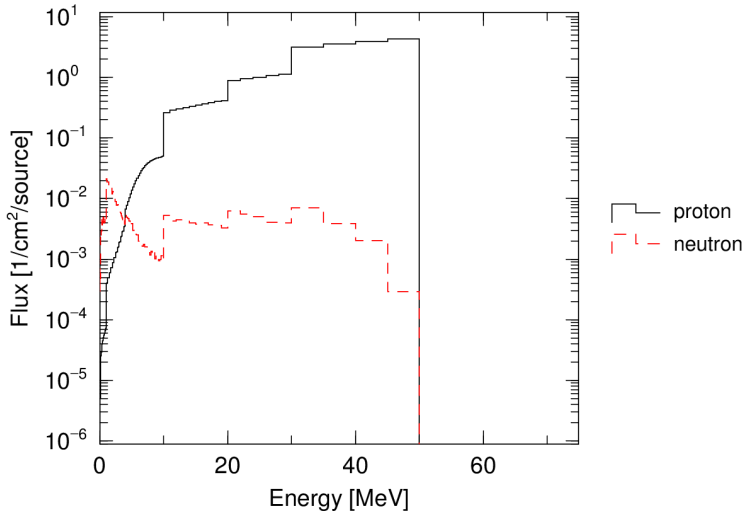


Figure A.9: Flux per source energy spectrum analysis inside a Tc-99 target with an 50 MeV proton beam.

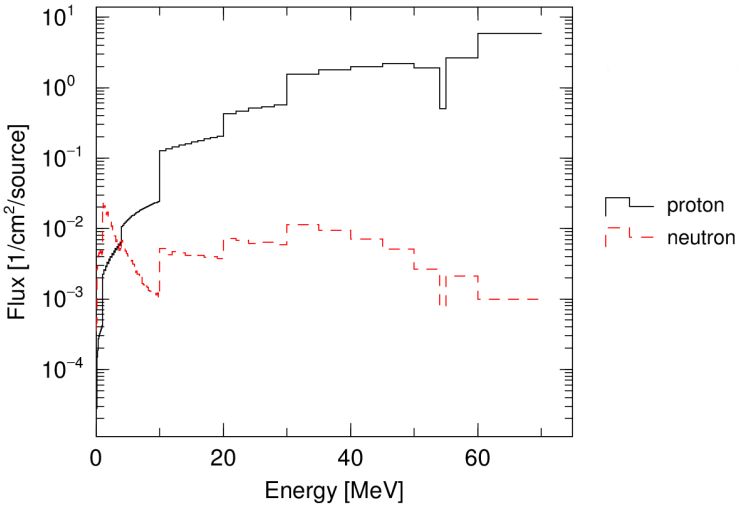


Figure A.10: Flux per source energy spectrum analysis inside a Tc-99 target with an 70 MeV proton beam.

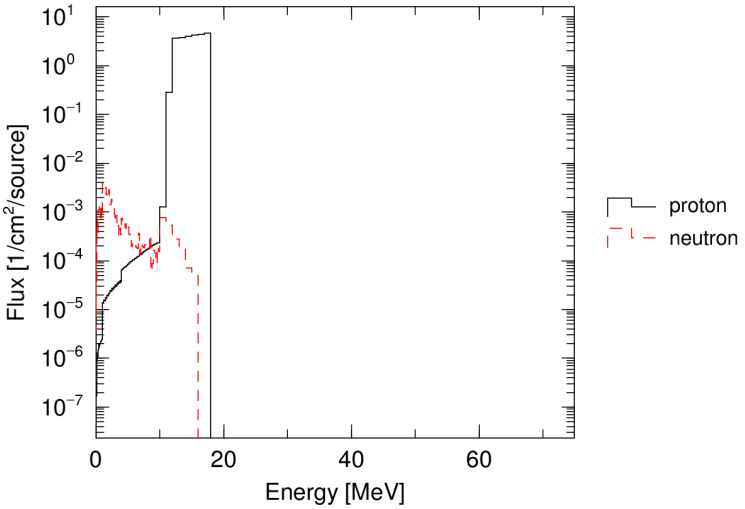


Figure A.11: Flux per source energy spectrum analysis inside an elemental tin target with an 18 MeV proton beam.

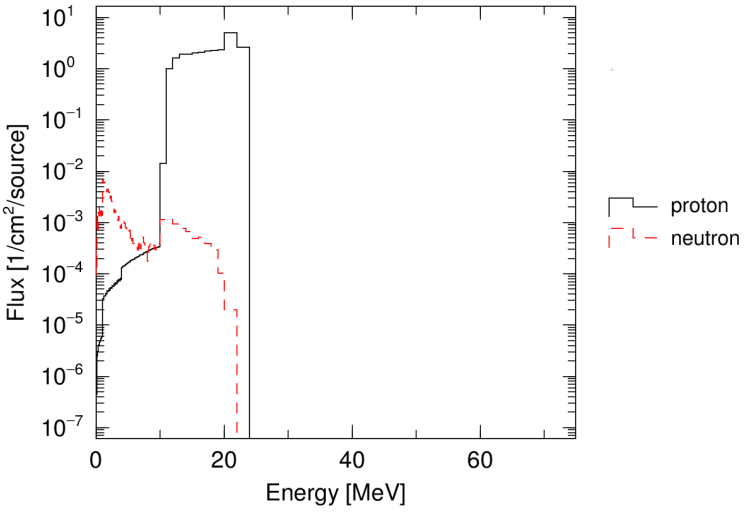


Figure A.12: Flux per source energy spectrum analysis inside an elemental tin target with an 23 MeV proton beam.

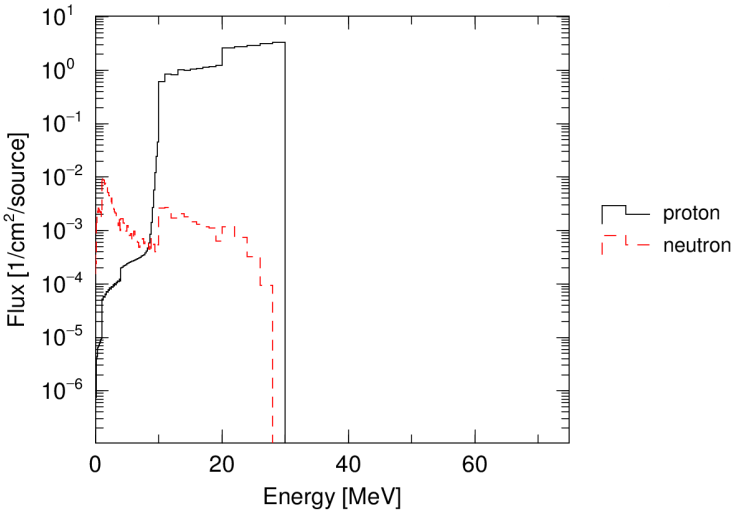


Figure A.13: Flux per source energy spectrum analysis inside an elemental tin target with an 30 MeV proton beam.

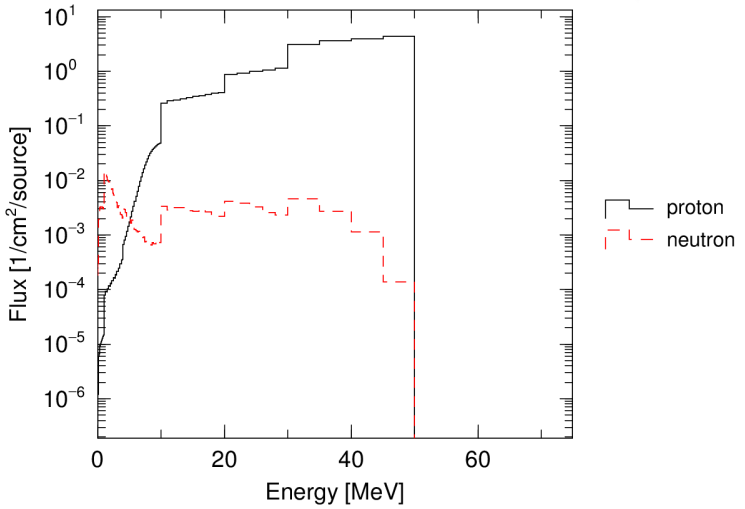


Figure A.14: Flux per source energy spectrum analysis inside an elemental tin target with an 50 MeV proton beam.

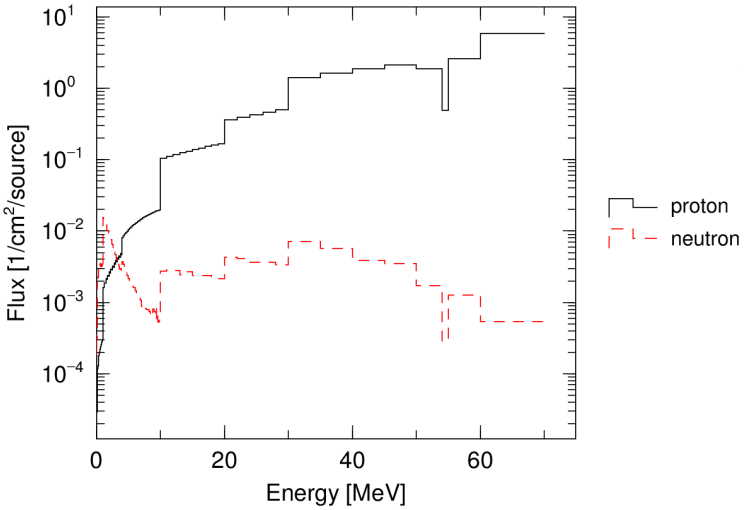


Figure A.15: Flux per source energy spectrum analysis inside an elemental tin target with an 70 MeV proton beam.

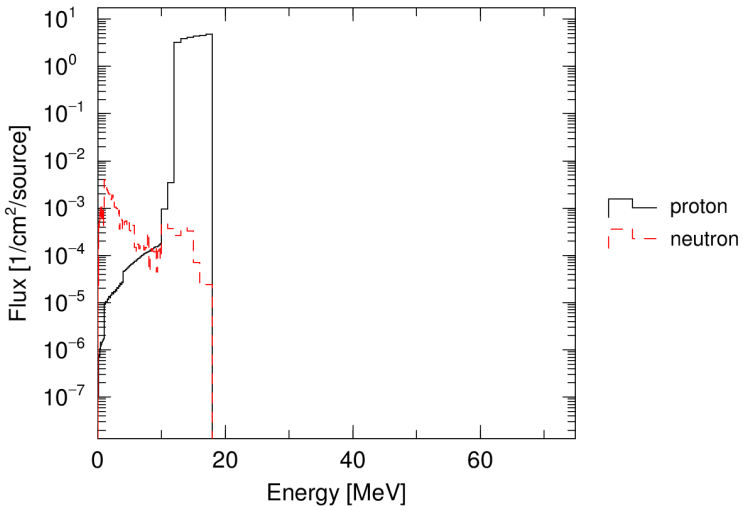


Figure A.16: Flux per source energy spectrum analysis inside a CsI compound target with an 18 MeV proton beam.

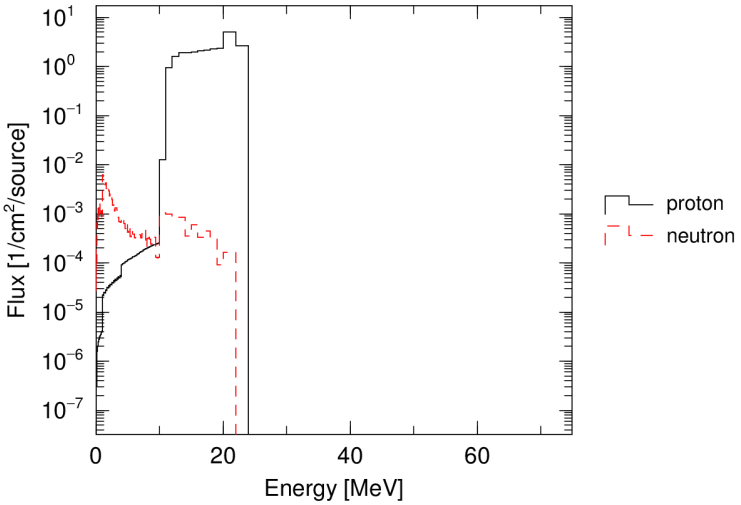


Figure A.17: Flux per source energy spectrum analysis inside a CsI compound target with an 23 MeV proton beam.

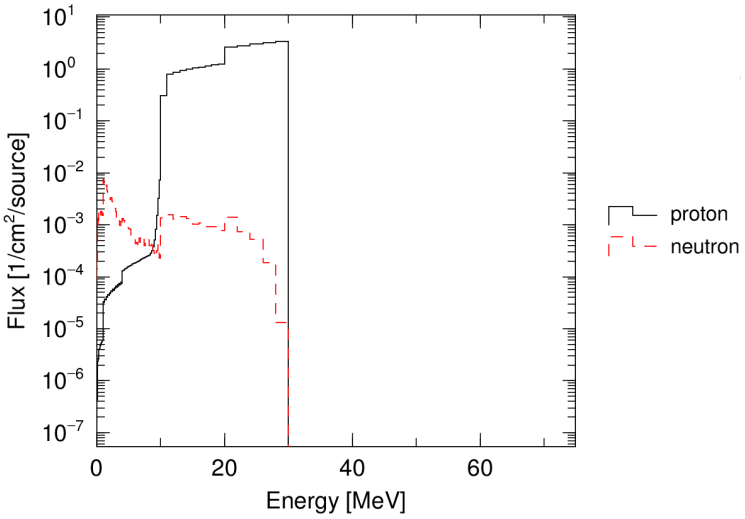


Figure A.18: Flux per source energy spectrum analysis inside a CsI compound target with an 30 MeV proton beam.

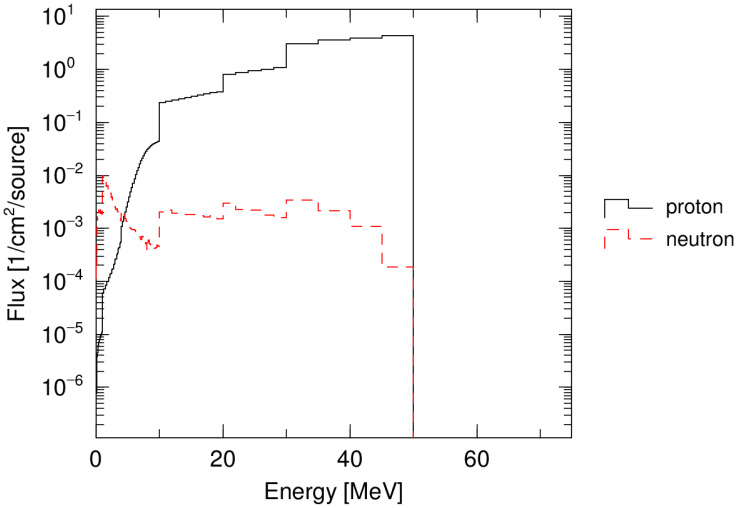


Figure A.19: Flux per source energy spectrum analysis inside a CsI compound target with an 50 MeV proton beam.

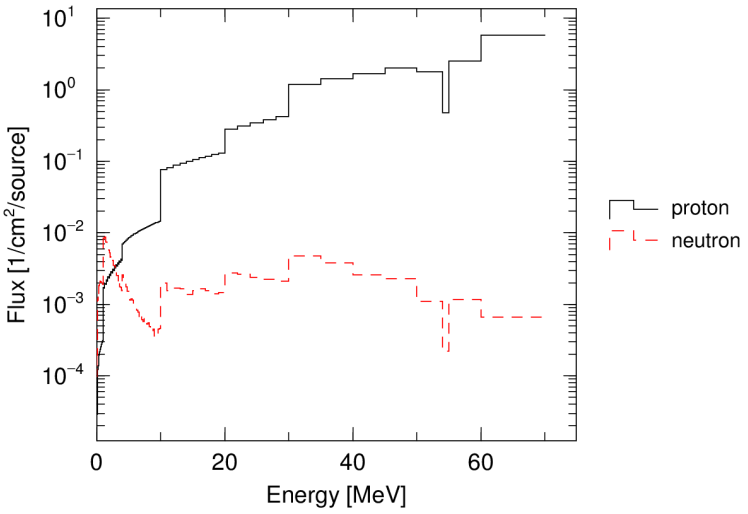


Figure A.20: Flux per source energy spectrum analysis inside a CsI compound target with an 18 MeV proton beam.

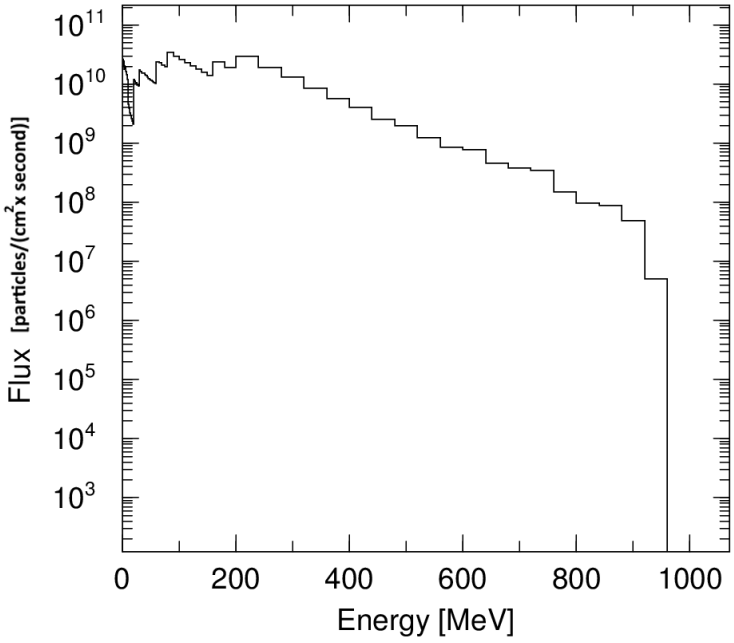


Figure A.21: Neutron flux per source energy spectrum analysis inside the elemental selenium LLFP pins. Note that the spallation target is composed of composed of Tc-99 and the beam energy is 1000 MeV. The source value of $6.25 \times 10^{16}$ protons/second attributed to a 10 mA beam is multiplied to the results.

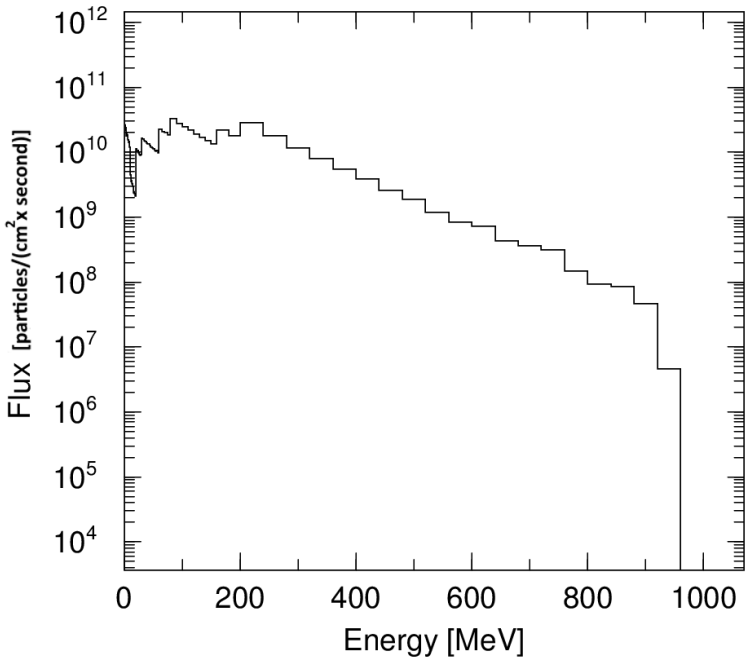


Figure A.22: Neutron flux per source energy spectrum analysis inside the elemental zirconium LLFP pins. Note that the spallation target is composed of composed of Tc-99 and the beam energy is 1000 MeV. The source value of $6.25 \times 10^{16}$ protons/second attributed to a 10 mA beam is multiplied to the results.

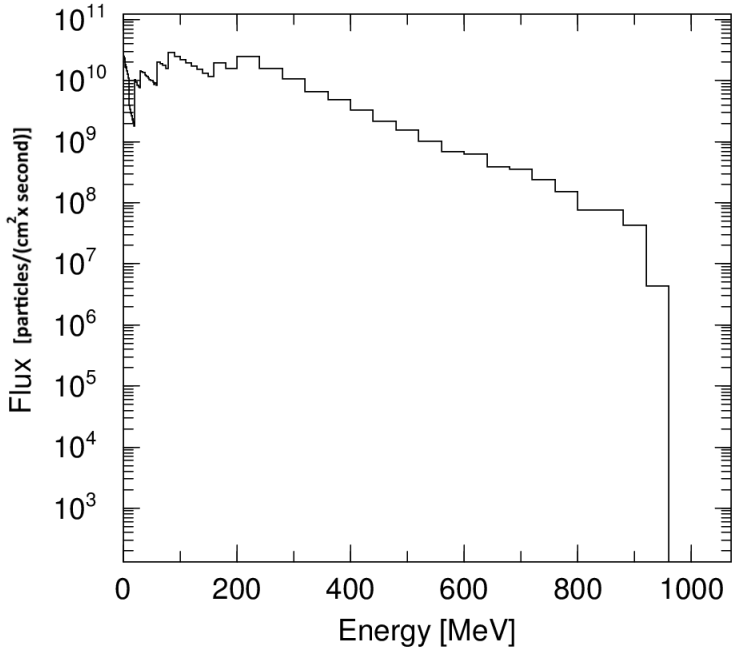


Figure A.23: Neutron flux per source energy spectrum analysis inside the Tc-99 LLFP pins. Note that the spallation target is composed of composed of Tc-99 and the beam energy is 1000 MeV. The source value of $6.25 \times 10^{16}$ protons/second attributed to a 10 mA beam is multiplied to the results.

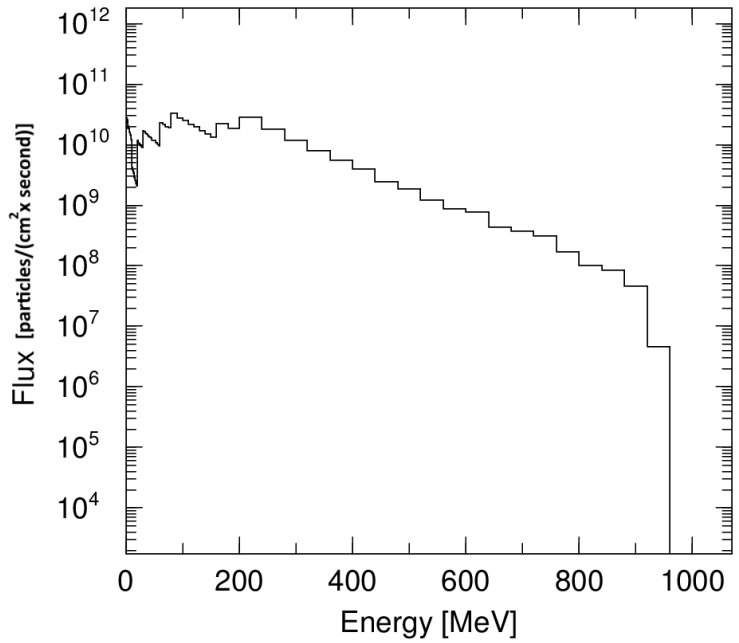


Figure A.24: Neutron flux per source energy spectrum analysis inside the elemental tin LLFP pins. Note that the spallation target is composed of composed of Tc-99 and the beam energy is 1000 MeV. The source value of $6.25 \times 10^{16}$ protons/second attributed to a 10 mA beam is multiplied to the results.

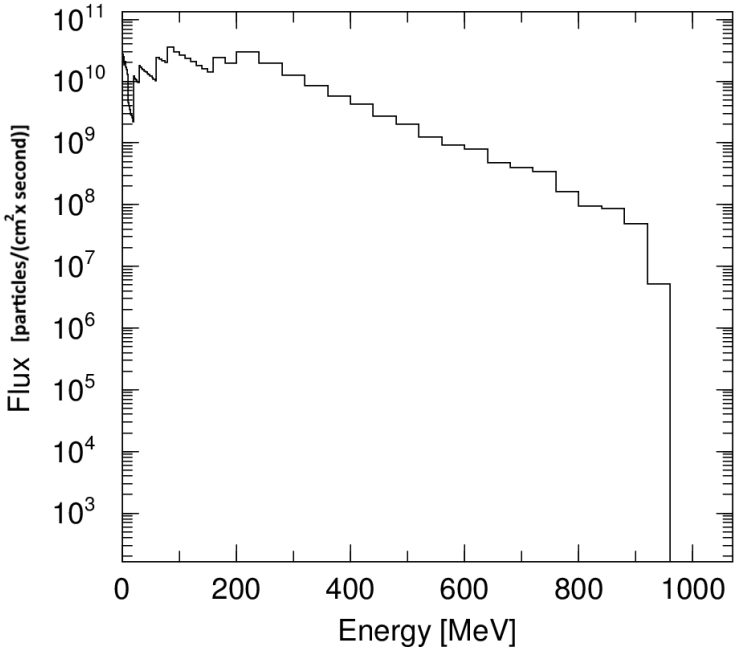


Figure A.25: Neutron flux per source energy spectrum analysis inside the CsI compound LLFP pins. Note that the spallation target is composed of composed of Tc-99 and the beam energy is 1000 MeV. The source value of $6.25 \times 10^{16}$ protons/second attributed to a 10 mA beam is multiplied to the results.

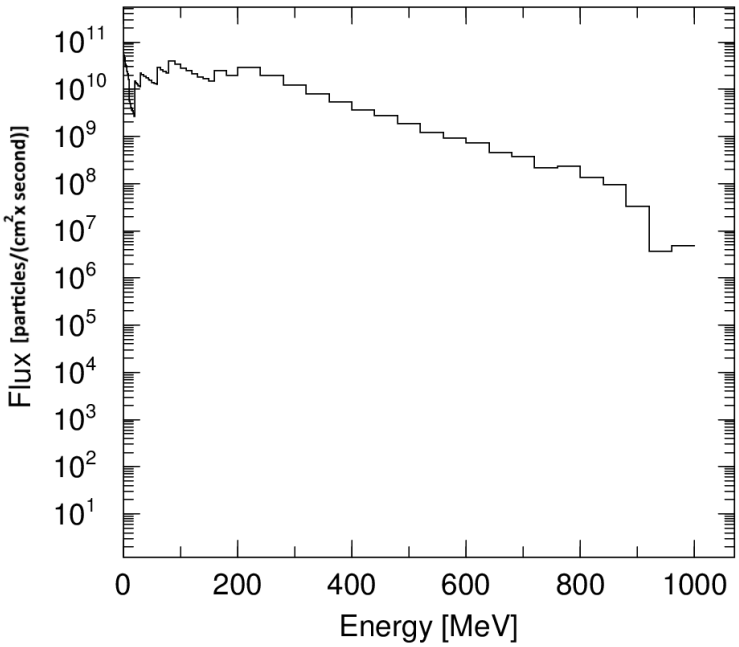


Figure A.26: Neutron flux per source energy spectrum analysis inside the elemental selenium LLFP pins. Note that the spallation target is composed of composed of lead and the beam energy is 1000 MeV. The source value of $6.25 \times 10^{16}$ protons/second attributed to a 10 mA beam is multiplied to the results.

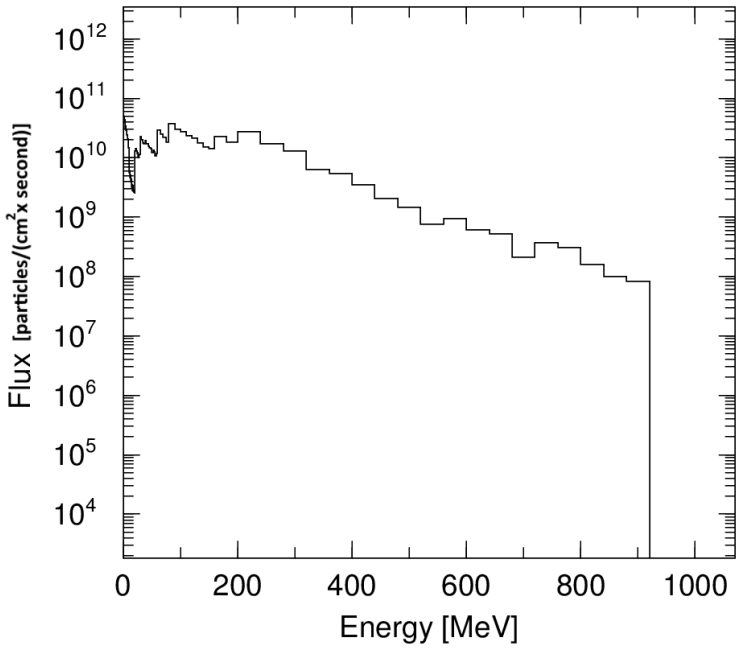


Figure A.27: Neutron flux per source energy spectrum analysis inside the elemental zirconium LLFP pins. Note that the spallation target is composed of composed of lead and the beam energy is 1000 MeV. The source value of $6.25 \times 10^{16}$ protons/second attributed to a 10 mA beam is multiplied to the results.

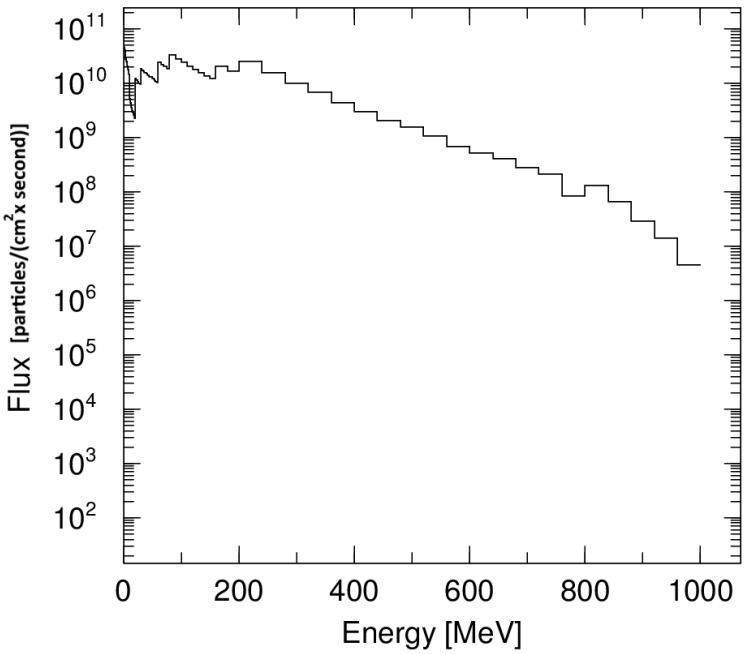


Figure A.28: Neutron flux per source energy spectrum analysis inside the Tc-99 LLFP pins. Note that the spallation target is composed of composed of lead and the beam energy is 1000 MeV. The source value of $6.25 \times 10^{16}$ protons/second attributed to a 10 mA beam is multiplied to the results.

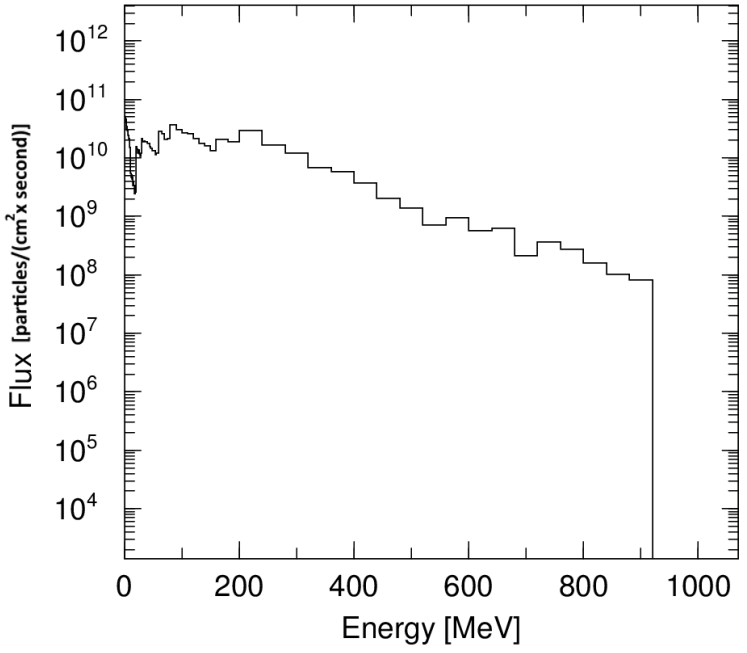


Figure A.29: Neutron flux per source energy spectrum analysis inside the elemental tin LLFP pins. Note that the spallation target is composed of composed of lead and the beam energy is 1000 MeV. The source value of $6.25 \times 10^{16}$ protons/second attributed to a 10 mA beam is multiplied to the results.

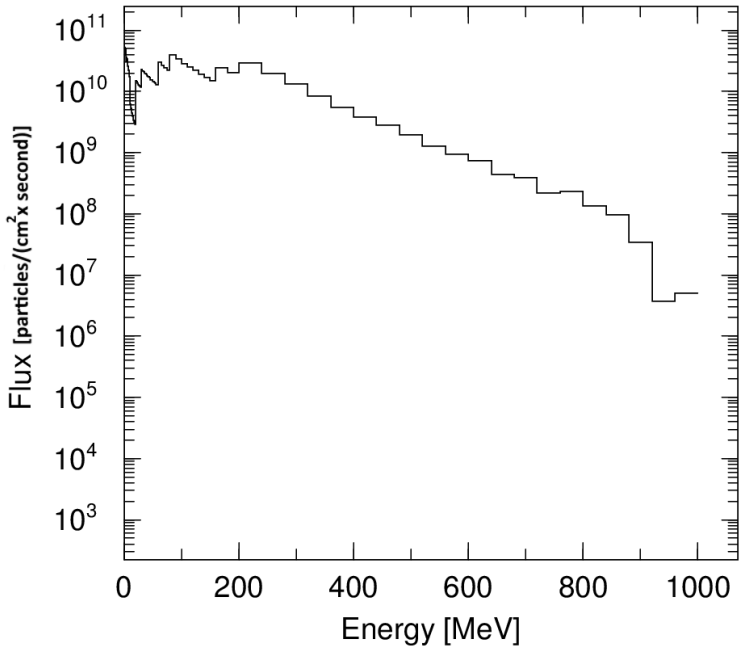


Figure A.30: Neutron flux per source energy spectrum analysis inside the CsI compound LLFP pins. Note that the spallation target is composed of composed of lead and the beam energy is 1000 MeV. The source value of $6.25 \times 10^{16}$ protons/second attributed to a 10 mA beam is multiplied to the results.

# References


[1] R. Wigeland, "Nuclear fuel cycle evaluation and screening – final report," *Idaho National Laboratory Report*, 2014. DOI: No.INL/EXT-14-31465.

[2] *Nuclear wallet cards*, Database, from the Brookhaven National Laboratory, 2019. URL: https://www.nndc.bnl.gov/wallet/wallet11.pdf.

[3] I. A. E. A. (IAEA). "Database of cyclotrons for radionuclide production." (), URL: https://nucleus.iaea.org/sites/accelerators/Pages/Cyclotron.aspx#InplviewHashd5afe566-18ad-4ac0-8aeb-ccf833dbc282=SortField%3DProton_x0020_Energy_x0020__x0028-SortDir%3DDesc. (accessed: 01.11.2024).

[4] T. Sato, Y. Iwamoto, S. Hashimoto, *et al.*, "Features of particle and heavy ion transport code system (phits) version 3.02," *Journal of Nuclear Science and Technology*, vol. 55, no. 6, 2018. DOI: 10.1080/00223131.2017.1419890. URL: https://doi.org/10.1080/00223131.2017.1419890.

[5] K. Amako, S. Guatelli, V. Ivanchencko, *et al.*, "Geant4 and its validation," *Nuclear Physics B - Proceedings Supplements*, vol. 150, pp. 44–49, 2006, Proceedings of the 9th Topical Seminar on Innovative Particle and Radiation Detectors, ISSN: 0920-5632. DOI: https://doi.org/10.1016/j.nuclphysbps.2004.10.083. URL: https://www.sciencedirect.com/science/article/pii/S0920563205008066.

[6] J.-C. Sublet, I. Hill, A. Trkov, R. Forrest, B. Mustin, and A. J. Koning, "FISPACT-II: An advanced simulation and inventory code for nuclear research and waste management," *Nuclear Data Sheets*, vol. 148, pp. 305–310, 2018. DOI: 10.1016/j.nds.2018.02.022. URL: https://www.sciencedirect.com/science/article/pii/S0090375218301342.

[7] W. S. Yang, Y. Kim, R. N. Hill, T. A. Taiwo, and H. S. Khalil, "Long-lived fission product transmutation studies," *Nuclear Science and Engineering*, vol. 146, no. 3, pp. 291–318, 2004. DOI: 10.13182/NSE04-A2411. eprint: https://doi.org/10.13182/NSE04-A2411. URL: https://doi.org/10.13182/NSE04-A2411.

[8] *Implications of Partitioning and Transmutation in Radioactive Waste Management* (Technical Reports Series 435). Vienna: INTERNATIONAL ATOMIC ENERGY AGENCY, 2004, ISBN: 92-0-115104-7. URL: https://www.iaea.org/publications/7112/implications-of-partitioning-and-transmutation-in-radioactive-waste-management.

[9] J. Kloosterman and L. Jianmang, *Transmutation of TC-99 and I-129 in fission reactors: A calculational study*. Netherlands Energy Research Foundation ECN, 1995.

[10] X. Y. Sun, L. H. Han, X. X. Li, B. L. Hu, W. Luo, and L. Liu, "Transmutation of mas and llfps with a lead-cooled fast reactor," *Scientific Reports*, vol. 13, no. 1, Jan. 2023. DOI: 10.1038/s41598-023-29002-3.

[11] T. Wakabayashi, "Transmutation characteristics of ma and llfp in a fast reactor," *Progress in Nuclear Energy*, vol. 40, no. 3, pp. 457–463, 2002, ISSN: 0149-1970. DOI: https://doi.org/10.1016/S0149-1970(02)00038-0. URL: https://www.sciencedirect.com/science/article/pii/S0149197002000380.

[12] S. Kapoor, "Accelerator-driven sub-critical reactor system (ads) for nuclear energy generation," *Pramana*, vol. 59, no. 6, pp. 941–950, Jan. 2002. DOI: 10.1007/s12043-002-0143-z.

[13] X. Y. Sun, W. Luo, H. Y. Lan, Y. M. Song, Q. Y. Gao, Z. C. Zhu, J. G. Chen, and X. Z. Cai, "Transmutation of long-lived fission products in an advanced nuclear energy system," *Scientific Reports*, vol. 12, no. 1, Feb. 2022. DOI: 10.1038/s41598-022-06344-y.

[14] K. Ismailov, K. Nishihara, M. Saito, and H. Sagara, "Optimization study on accelerator driven system design for effective transmutation of iodine-129," *Annals of Nuclear Energy*, vol. 56, pp. 136–142, 2013, ISSN: 0306-4549. DOI: https://doi.org/10.1016/j.anucene.2013.01.042. URL: https://www.sciencedirect.com/science/article/pii/S0306454913000595.

[15] K. Imasaki, D. Li, S. Miyamoto, S. Amano, T. Motizuki, and Y. Asano, "Gamma-ray beam transmutation," *Energy Conversion and Management*, vol. 49, no. 7, pp. 1922–1927, 2008, ICENES'2007, 13th International Conference on Emerging Nuclear Energy Systems, June 3–8, 2007, İstanbul, Turkiye, ISSN: 0196-8904. DOI: https://doi.org/10.1016/j.enconman.2007.09.030. URL: https://www.sciencedirect.com/science/article/pii/S0196890407004359.

[16] J. Chen, W. Xu, H. Wang, *et al.*, "A potential photo-transmutation of fission products triggered by compton backscattering photons," *Nuclear Instruments and Methods in Physics Research Section A: Accelerators, Spectrometers, Detectors and Associated Equipment*, vol. 599, no. 1, pp. 118–123, 2009, ISSN: 0168-9002. DOI: https://doi.org/10.1016/j.nima.2008.10.031. URL: https://www.sciencedirect.com/science/article/pii/S0168900208015842.

[17] J. M. Schippers, "Cyclotrons for particle therapy," en, *CERN Yellow Reports: School Proceedings*, Vol 1 (2017): Proceedings of the CAS–CERN Accelerator School on Accelerators for Medical Applications, 2017. DOI: 10.23730/CYRSP-2017-001.165. URL: https://e-publishing.cern.ch/index.php/CYRSP/article/view/61.

[18] "Cost/benefit comparison for 45 mev and 70 mev cyclotrons," May 2005. URL: https://www.osti.gov/biblio/1299047.

[19] G. J. Russel, *Spallation physics - an overview*. URL: https://inis.iaea.org/collection/NCLCollectionStore/_Public/23/015/23015552.pdf.

[20] P. Böni, "Neutron sources," in *Encyclopedia of Condensed Matter Physics (Second Edition)*, T. Chakraborty, Ed., Second Edition, Oxford: Academic Press, 2024, pp. 443–459, ISBN: 978-0-323-91408-6. DOI: https://doi.org/10.1016/B978-0-323-90800-9.00126-8. URL: https://www.sciencedirect.com/science/article/pii/B9780323908009001268.

[21] J. Alonso, "The spallation neutron source project," *Proceedings of the 1999 Particle Accelerator Conference (Cat. No.99CH36366)*, 1999. DOI: 10.1109/pac.1999.795764.

[22] C. Baumgarten, M. Seidel, A. Adelmann, *et al.*, "Production of a 1.3 mw proton beam at psi," Jun. 2010.

[23] V. Yakovlev, J. Grillenberger, S.-H. Kim, M. Seidel, and M. Yoshii, "The energy efficiency of high intensity proton driver concepts," May 2017. DOI: 10.18429/JACoW-IPAC2017-FRXCB1. URL: https://www.osti.gov/biblio/1421547.

[24] T. Sato, K. Niita, N. Matsuda, *et al.*, "Overview of particle and heavy ion transport code system phits," *Annals of Nuclear Energy*, vol. 82, pp. 110–115, Aug. 2015. DOI: 10.1016/j.anucene.2014.08.023.

[25] S. Agostinelli, J. Allison, K. Amako, *et al.*, "Geant4—a simulation toolkit," *Nuclear Instruments and Methods in Physics Research Section A: Accelerators, Spectrometers, Detectors and Associated Equipment*, vol. 506, no. 3, pp. 250–303, Jul. 2003. DOI: 10.1016/s0168-9002(03)01368-8.

[26] URL: https://www.oecd-nea.org/janisweb/.

[27] 2007. URL: https://phits.jaea.go.jp/OvMapOfModels.html.

[28] D. Mancusi, A. Boudard, J. Cugnon, J. .-. David, P. Kaitaniemi, and S. Leray, "Extension of the liège intranuclear-cascade model to reactions induced by light nuclei," *Physical Review C*, vol. 90, p. 054 602, 2014. URL: https://api.semanticscholar.org/CorpusID:54216742.

[29] C. Wickert, personal communication, 2024.

[30] J. Ayres and C. Trilling, "Heavy water and organic fluids as neutron moderator and reflector materials," *Nuclear Engineering and Design*, vol. 14, no. 3, pp. 363–389, 1971, ISSN: 0029-5493. DOI: https://doi.org/10.1016/0029-5493(70)90158-5. URL: https://www.sciencedirect.com/science/article/pii/0029549370901585.

[31] H. H. Hausner, "Beryllium as a moderator and reflector for nuclear reactors," *Beryllium*, Dec. 1965. DOI: 10.1525/9780520338821.

[32] K. Shibata, O. Iwamoto, T. Nakagawa, *et al.*, "Jendl-4.0: A new library for nuclear science and engineering," *Journal of Nuclear Science and Technology*, vol. 48, no. 1, pp. 1–30, 2011. DOI: 10.1080/18811248.2011.9711675. eprint: https://doi.org/10.1080/18811248.2011.9711675. URL: https://doi.org/10.1080/18811248.2011.9711675.